Template Directed Growth of Nb doped $SrTiO_3$ using Pulsed Laser Deposition

Gordon Waller

Thesis submitted to the faculty of the
Virginia Polytechnic Institute and State University
in partial fulfillment of the requirements for the degree of

Masters of Science

in
Materials Science and Engineering

Jeremiah T. Abiade, Chair
Guo Quan Lu
Kathy Lu

April 29, 2011
Blacksburg, VA

Keywords: Pulsed Laser Deposition, Electron Beam Lithography, Oxide nano-patterning

Template Directed Growth of Nb doped $SrTiO_3$ using Pulsed Laser Deposition

Gordon Waller

ABSTRACT

Oxide materials display a wide range of physical properties. Recently, doped complex oxides have drawn considerable attention for various applications including thermoelectrics. Doped complex oxide materials have high Seebeck coefficients (S) and electrical conductivities (σ) comparable to other doped semiconductors but low thermoelectric figure of merit ZT values due to their poor thermal conductivities. For example, niobium doped strontium titanate ($SrNb_xTi_{1-x}O_3$ or simply Nb:STO) has a power factor comparable to that of bismuth telluride. Semiconductor nanostructures have demonstrated a decrease in thermal conductivity (κ) resulting in an increase in the thermoelectric figure of merit (ZT). Nanostructures of doped oxides like niobium doped strontium titanate, may also lead to decreased κ and a corresponding increase in ZT. The major impediment to nanostructured oxide thermoelectric materials is the lack of suitable fabrication techniques for testing and eventual use. Electron Beam Lithography (EBL) was used to pattern poly-methyl-methacrylate (PMMA) resists on undoped single crystalline $SrTiO_3$ (STO) substrates which were then filled with Nb:STO using Pulsed Laser Deposition (PLD) at room temperature. This technique produced nanowires and nanodots with critical dimensions below 100 nm, and a yield of approximately 95%. In addition to scanning electron microscopy and atomic force microscopy morphological studies of the patterned oxide, thin film analogues were used to study composition, crystallinity and electrical conductivity of the material in response to a post deposition heat treatment. Since the thin films were grown under similar experimental parameters as the oxide nanostructres, the patterned oxides are believed to be stoichiometric and highly crystalline. The study found that using a combination of EBL and PLD, it is possible to produce highly crystalline, doped complex oxide nanostructures with excellent control over morphology. Furthermore, the technique is applicable to nearly all

materials and provides the capability of patterning doped oxide materials without the requirement of etching or multiple lithography steps makes this approach especially interesting for future fundamental materials research and novel device fabrication.

Acknowledgements

I would like to acknowledge some of the major sources of aid to me during my work towards this thesis – Dr. Aaron Stein at Brookhaven National Lab for his help with electron beam lithography, the staff members at the Nanoscale Characterization and Fabrication Laboratory (John McIntosh, Dr. Jerry Hunter, and Steve McCartney), Hari Krishna who assisted me in testing electrical conductivity, and of course my advisor Dr. Jeremiah Abiade.

Thank you to everyone who assisted me during my research – because of the availability of talented scientists and mentors at Virginia Tech, I have received an excellent education and a strong base for a career as a research engineer.

Table of Contents

List of Figures

List of Tables

List of Equations

Chapter 1: Introduction

Thermoelectric materials have provided an interesting opportunity for many years of materials research as they offer an elegant solution to the often discussed energy crisis. The promise of electrical energy generation from a solid state device for nothing more than a thermal gradient is an understandably desirable goal. Indeed, given that most heat producing systems are simply interested in heat dissipation thermoelectric power generation offers a potentially advantageous alternative. However, not all thermoelectric materials and devices are made equal. Metals, intrinsic semiconductors, and doped oxide ceramics can all display the thermoelectric effect, which is simply defined as a voltage gradient produced in response to a temperature gradient or vice versa. These qualities, as well as the rate at which the thermoelectric conversion occurs are described by the Seebeck effect, Peltier effect and Thompson effect respectively (1). More important is the relative comparison between thermoelectric materials, which is achieved by introducing the concept of the Figure of Merit, defined below:

$$Z = \frac{\sigma S^2}{k} \qquad (Eq. 1).$$

Where σ is electrical conductivity with units of Siemens per meter (S/m), k is thermal conductivity with units of Watts per meter per degree Kelvin (W/m-K), and S is the Seebeck coefficient with units of volts per degree Kelvin (V/K). Through unit manipulation it can be seen that the figure of merit Z has units of 1/K, and is therefore often multiplied by the average temperature T to become unitless, expressed simply as ZT. Furthermore, the maximum theoretical efficiency of a thermoelectric device can be described by the following equation:

$$Max\ Efficiency = \eta\gamma \qquad (Eq. 2)$$

Where η is the Carnot efficiency from thermodynamics, defined as

$$\eta = 1 - \frac{T_{cold}}{T_{hot}} \qquad (Eq. 3)$$

and γ is the material specific efficiency defined as

$$\gamma = \frac{\sqrt{1 + Z\left(\frac{T_{hot} + T_{cold}}{2}\right)} - 1}{\sqrt{1 + Z\left(\frac{T_{hot} + T_{cold}}{2}\right)} + \frac{T_{cold}}{T_{hot}}} \qquad (Eq. 4).$$

With the consideration of the maximum efficiency equation, it is clear that to improve the maximum efficiency of any thermoelectric device either the Carnot efficiency or material efficiency (or

both) must be improved. Improvement to the Carnot efficiency is the most obvious. The larger the difference between T_{hot} and T_{cold} , generally referred to as ΔT , the closer η is to 1. While in general the largest ΔT possible is desired for maximum performance of a thermoelectric device, ZT for each thermoelectric material is strongly temperature dependent. Take for example, the commonly used thermoelectric material bismuth telluride (Bi_2Te_3) which has a peak reported ZT value of .87 at 300 K, which quickly drops with a temperature change in any direction (1). So, while a very large ΔT could be generated in many scenarios (for example the dissipated heat from a car engine compared to the ambient), the average temperature would place the ZT value well out of his peak efficiency range.

The challenge now becomes not where the largest ΔT value can be obtained, but how to achieve a large Z value that occurs at an appreciably elevated average temperature. By inspection of equation 1, we find that this can be accomplished by increasing σ or S, or by decreasing k. The Seebeck coefficient describes the separation of charge carriers during an applied temperature gradient. A large amount of charge carriers available to migrate away from the hot end of a thermoelectric element creates this separation and establishes a voltage gradient. The sign of the Seebeck coefficient denotes what type of majority charge carriers are responsible for the charge separation, electrons producing negative values of S and holes producing positive values. Metals have the largest number of charge carriers and very high σ, however both holes and electrons are present during electrical transport. Thus, S tends to be lower for metals. Furthermore, the charge carriers in metals also contribute to increase k. Doped ceramics (semiconductors) offer the best combination of thermoelectric properties. Tightly bound valence electrons restrict the thermal conductivity to lattice contributions, or phonons, and dopant atoms restrict the majority carrier species by selectively using donors or acceptors as well as increasing electrical conductivity. While generally much lower than the ZT value for telluride compounds, larger band gap semiconductors have peak values at higher temperatures.

Despite the advantages of using semiconductors for thermoelectric devices, their values of ZT are still much too low for effective application. While individual parameters can be affected by doping, composition and crystal structure, all three are critically interrelated. Larger σ lead to decreased S and increased k and vice versa. An alternative approach to manipulating ZT is needed. One such approach that is the topic of this report is nanostructuring. By introducing nanoscale constraints in a thermoelectric material, the key properties can be individually controlled. A common area of research is into methods to reduce thermal conductivity while leaving electrical conductivity unchanged. This can be achieved in semiconductors by interrupting the migration of phonons. Nanowires, nanoscale composites and multilayered heterostructures are the key areas of research in this approach. Furthermore, doped oxide materials which satisfy the condition of high temperature capability are currently the focus of many

fundamental thermoelectric materials studies. However, difficulty in producing oxide nanostructures necessitates research into new techniques for their fabrication. Conventional techniques can only produce undoped oxide materials or require complicated and expensive patterning techniques. In this thesis, a simple template filling approach is used to create doped oxide nanostructures with dimensions on the order of 100 nanometers. Fabrication of these structures is the first step in realizing the optimization of ZT parameters for oxide semiconductors.

Chapter 2: Literature Review

2.1 Advances in Thermoelectric Materials

The study of thermoelectricity began in 1826 with the discovery of the Seebeck effect by Thomas Johann Seebeck. Initially the effect was observed for junctions of dissimilar metals, but the description of the thermoelectric Figure of Merit by Edmund Altenkirch in 1911 led the way for the use of semiconductors as superior thermoelectric materials, as it allowed a direct comparison of thermoelectric efficiency between materials. While relatively low efficiency thermoelectric devices have found uses as thermocouples and radioisiotope thermoelectric generators, high efficiency materials have evaded discovery. A discussion of modern thermoelectric devices and materials could perhaps begin with Bi_2Te_3.

In 1954 the General Electric Corporation published their findings on the use of Bi_2Te_3 and other semiconductor thermoelectric materials for the application of refrigeration (2). Despite the fact that the basis of the thermoelectric effect had been first observed over 100 years prior, the efficiency of studied materials had proven too low to create a realistic thermoelectric cooler. Early research was erroneously aimed at maximizing the ratio of electrical to thermal conductivity, and thus metals were the focus of these works. While important, this ratio alone negated to consider the contribution of the Seebeck coefficient, which is typically small for metals. In fact, the authors of the General Electric report, Goldsmid and Douglas, state that for the metallic materials typically used for thermocouples, the effects of Joule heating overcame that of the Peltier cooling effects. In their work, Goldsmid and Douglas identified a critical aspect of thermoelectric performance of semiconductors, which is that phonons, rather than electrons as in metals, are the principal carriers of thermal energy. By capitalizing upon this understanding, the researchers determine that semiconductors with high atomic weights, in addition to acceptably high electrical conductivities and Seebeck coefficient, will aid in thermoelectric efficiency by decreasing thermal conductivity. Their work resulted in p-type doped bulk bismuth telluride with a ZT of .51. In their concluding statements, the progenitors of thermoelectric materials research predict that greater ZT values will be needed in the future for applications in cooling as well as energy harvesting.

By 1968 the field of thermoelectric materials research was such that many avenues had been pursued. In a review article written by F.D. Rosi of the former Radio Corporation of America, a detailed description of the materials progress up to that point was given (3). Telluride compounds, including Bi_2Te_3 investigated by Goldsmid and Douglas, represent one area of heavy research at the time. In his review, Rosi points out not only the importance of the high ZT but also describes the interrelationships between the constituent factors, which at this point had created a ceiling on the performance of thermoelectric materials. For example, while doping of a semiconductor can increase the Seebeck

coefficient and electrical conductivity by increasing the Fermi level, this eventually leads to degeneracy. Degenerate semiconductors then experience a decrease in thermopower (σS^2) as well as an increase in electron dominated thermal conductivity. Furthermore, Rosi highlights the importance of both a high melting temperature and large band gap to maximize performance at high temperatures. In addition to the tellurium based alloys, alloys of Si and Ge as well as compound semiconductor GaAs were also gaining popularity as these materials satisfied the requirements of high melting temperature and large band gap (compared to the tellurides). These materials saw ZT values slightly above 1 at temperatures in the range of 800 °C, which was in stark contrast to the ZT of .66 for p-type and .84 for n-type Bi_2Te_3 at only 57 °C.

For applications of thermoelectric devices, both Goldsmid and Rosi saw outer space as the ideal setting. Electrical power generation from a radioisotope thermal source presented advantages over solar power for deep space exploration, as it still does today. However the ZT and optimum temperatures of the materials discussed still presented efficiencies too low for terrestrial applications. Specifically, thermoelectric devices would have to compete with fossil fuel based methods of power generation. With this consideration new materials and techniques have been implemented. The remainder of this literature review will focus on the following: First, the progress made in the nano-structuring of materials for application in thermoelectrics, and second, the field of oxide thermoelectric materials and the methods used to pattern oxide materials. The combination of these concepts is the goal of the present work.

2.2 Nanostructuring of Thermoelectric Materials

2.2.1 3D Nanostructures

Nanostructuring provides opportunities for manipulation of individual properties related to thermoelectric performance, while doping and other compositional changes tend to affect all properties. A nanostructure or nanomaterial is defined as having one or more principal dimensions (length, width or height) less than 100 nm. Significant changes in the mobility of electrons, phonons and entire atoms can be affected at this scale. The nanostructuring approach is most easily visualized as discrete entities; that is particles, wires and films. However, bulk materials can also benefit from nanostructuring. Two schools of thought are prevalent in field of bulk nanostructured materials, both of which strive to maximize electrical conductivity and minimize thermal conductivity through physical mechanisms, namely the preferential scattering of phonons over electrons. The first method is best embodied by the research into skutterudite typed minerals. Skutterudite typed minerals are characterized by a large void volume in each unit cell. As pure materials, skutterudites showed some promise as thermoelectric materials (4) as they

contain heavy atoms and large unit cells which were identified as beneficial to reducing κ by Goldsmid and Douglas in the 1950s. The thermoelectric performance of these structures shows a dramatic increase when the unit cells are further optimized for reducing phonon migration by introducing an additional atom, typically a heavy rare earth element, into the void space formed in the unit cells of these structures. Materials of this type are described as being "electron crystals" and "phonon glass" as they (ideally) conduct electrons like a crystalline solid and phonons like an amorphous glass. These filled skutterudites, with the general form TM_4B_{12} in which T is a rare earth element, and M and B represent group 8 and group 15 atoms respectively, have been researched extensively. Morelli and Meisner reported an order of magnitude reduction in κ for the filled skutterudite $CeFe_4Sb_{12}$ compared to other unfilled skutterudites at the same temperature (5), however subsequent work has shown that while thermal conductivity is reduced by the "rattling" of the rare earth ions, they also act as charge centers that decrease electrical conductivity (6) (7) (8).

The second approach to nanostructuring of bulk thermoelectric relies on nanoscale inclusions or secondary phases, however their conceptual application is very similar to the skutterudite materials as the goal is to increase electrical conductivity or reduce thermal conductivity (or both) without invoking changes in stoichiometry or chemical bonding of the main thermoelectric phase. An early attempt at this approach was made by Scoville et. Al in which nanophase inclusions of boron nitride and other inert compounds on the order of only 4 nm were introduced into a SiGe matrix (9). While their intent was to reduce thermal conductivity by phonon scattering, the nanophases also served to decrease grain boundary mobility (and thus grain size) which led to a decrease in electrical conductivity as well. Similar results were found in Bi/Bi-SiO_2 nanocomposites (10).

2.2.2 2D Nanostructures

While often requiring more complicated fabrication methods than bulk techniques, thin films offer additional opportunities to maximize ZT for thermoelectric materials. Phonon scattering, the primary mechanism described for enhancement of ZT for bulk materials is one possibility, but quantum confinement of charge carriers (and thus manipulation of the power factor σS^2) is also possible. Furthermore, studies of well characterized bulk thermoelectric materials (chiefly Bi_2Te_3 and its' alloys) in thin film form are common as films can eliminate stoichiometric and crystallographic defects that plague the performance of bulk thermoelectric materials.

In monolayer films mixed results have been found. For bismuth telluride based systems, Makala found a decrease in the Seebeck coefficient compared to the bulk (11), while Tan observed an increase (12). However each of these sources indicates an extreme sensitivity of the thermoelectric performance to

film quality. Zahid and Lake have shown in their theoretical work that a single "quintuple layer" consisting of only 5 atomic layers of alternating Bi and Te would result in a massive change in the electron band structure and a corresponding increase in the figure of merit (13). Cleary making such a film would require an extreme level of experimental control.

Layers of alternating films, called super-lattice or heterostructures, have also been researched. In 1995 Whitlow and Hirano suggested that a super lattice of $Si_{80}Ge_{20}$ and an insulating interlayer could result in an increased electrical conductivity compared to bulk samples by restricting the migration of low energy charge carriers in vertically stacked quantum wells (14). While structurally different, their hypothesis is very similar to the approach later followed by Zahid and Lake. Another similarity between the works is the finding that the film thickness, either for a super-lattice or quintuple layer, must be on the order of a single unit cell. The obvious advantage in this case for the super-lattice is that the effect can be maintained with a larger (and easier to fabricate) device, *i.e.* a super-lattice repeated hundreds of times. Super-lattice structures have already been shown to be effective as spot coolers in microelectronics (15) (16) (17) and show potential as thermoelectric generators (17).

2.2.3 1D Nanostructures

The final nanostructures for consideration are one dimensional nanostructures, or more often referred to as nanowires. As detailed by Dresselhaus in 1999, nanowires experience a quantum confinement effect analogous to that predicted for films, which manipulates the charge carrier density of states (18). What was perhaps most significant about her findings however was that the minimum dimension to first observe the quantum confinement (and the associated semi-metal to semiconductor transition for Bismuth) was on the order of 50 nm, which was much more practical than the Ångstrom scale requirement of films and super lattices. Arrays of Bi_2Te_3 wires with dimensions on the order of 50 nm have been fabricated by several methods, but have not demonstrated the predicted increase in thermoelectric performance (19) (20). Li *et. Al.* showed in a particularly powerful demonstration of 1D nanostructures with a thermal conductivity for 58 nm Si/SiGe super lattice nanowires of less than half that of film super lattices of the same composition (21). They suggested that in addition to the boundary scattering of phonons, an alloy scattering effect further reduced thermal conductivity in their nanowires. Boukai *et. Al.* have even been successful at directly measuring the ZT of arrays of 20 nm Si nanowires on a Si substrate, reporting an increase of 100 times compared to bulk Si (22).

2.3 Oxide Thermoelectric Materials: Nb:STO

2.3.1 Advantages of Oxide Thermoelectrics

As discussed in the previous section, the performance of a thermoelectric material can be enhanced by either increasing the thermopower ($S^2\sigma$), or decreasing the thermal conductivity, κ. Semiconductors provide the best opportunity for maximizing thermopower, however in traditional semiconductors such as Si high levels of doping often lead to off-site doping and degeneracy. Oxide semiconductors, of which STO is the premier example, have high solid solubility of dopant atoms and extremely high Seebeck coefficients, but with relatively large thermal conductivities and thus very low values of ZT. However, their electrical conductivities still limit their implementation as a thermoelectric material. Regardless, a significant amount of research has been devoted to this compound as it is capable of application in high temperature scenarios where stability and a high melting point are desired (23).

2.3.2 3D Nanostructures of Nb:STO

Bulk (3D) nanostructuring techniques have been heavily investigated for the reduction of κ in doped and undoped STO. Hiromichi Ohta, Kunihito Koumoto and their colleagues have been especially prolific in this field. Originally their work focused on the intrinsic super lattice reminiscent formations in STO known as the Ruddlesden-Popper phase. In the Ruddlesden-Popper phase, layers of SrO form between layers of STO in individual crystallites. By studying the effect of Nb dopant concentration on the bonds Ti-O_6 octahedron formed in the STO unit cell, ratio of SrO to STO layers, and size of the impurity dopant atom Ohta and Koumoto could manipulate the thermal conductivity resulting in an increased ZT (24) (25). Koumoto, in collaboration with the University of Electronic Science and Technology of China, has published many articles researching the effect of nanostructure on bulk STO samples. By introducing thermally insulating phases in a solid state reaction with Nb doped STO, Koumoto et Al. showed that the thermal conductivity of the doped oxide could effectively be reduced from the bulk value (26) (27). Several compounds were demonstrated to be effective, however the most significant improvement was found by the addition of 3 wt% Potassium Nitrate nanowires with a diameter of 20-40 nm and lengths of hundreds of nanometers (28). The potassium nitrate nanowires not only served as phonon scattering centers to decrease thermal conductivity, but also served to increase grain growth and as a direct result increase electrical conductivity. The same authors went on to investigate directly the effect of grain size on thermal conductivity in an undoped STO ceramic. Their findings indicate that interfacial thermal resistance, known as the Kapitza resistance, is more influential than phonon scattering (29). The following expression was used to calculate the mean free path for phonons assuming thermal conductivity is limited to the lattice thermal conductivity contribution, which was found to be an order of magnitude

smaller than the 55 nm grain size STO, which also observed the strongest reduction in thermal conductivity.

$$l_{ph} = \frac{3\kappa_L}{C_v v_m} \qquad (Eq. 5)$$

Where κ_L is the lattice thermal conductivity, C_v is the constant volume heat capacity, and v_m is the average speed of sound in the material. The thermal conductivity as a function of the Kapitza resistance can be calculated as follows.

$$\kappa = \frac{\kappa_0}{1 - \frac{\kappa_0 R_\kappa}{d}} \qquad (Eq. 6)$$

For single crystals, Ohta and Koumoto found that while doping concentration strongly affected both electrical conductivity and Seebeck coefficient, thermal conductivity was largely unchanged (30).

2.3.3 2D Nanostructures of Nb:STO

Films, or 2D nanostructures, have also been grown for Nb:STO. The most common methods used are Pulsed Laser Deposition (PLD) and Molecular Beam Epitaxy (MBE). Both methods have been shown to be capable of producing epitaxial films with high electrical conductivity and low surface roughness (31) (32). Typically a stoichiometric target is used in a high vacuum or partial oxygen pressure environment. When deposited on compatible oxide substrates such as $LaAlO_3$ (LAO) or even STO for homoepitaxial growth the surface roughness can be as low as .25 nm and electrical conductivity on the order of 10^{-4} Ω-cm. The formation of oxygen vacancies is common during growth of oxide materials by PLD, and as a result the deposition environment (substrate temperature, deposition rate and chamber pressure and epitaxial strain) are extremely important. Manipulation of these parameters has been found to affect the lattice constant as well as electrical conductivity and surface roughness (33) (34). Ohta and Koumoto, previously mentioned for their work with bulk STO, have also been active in the field of thin film STO. They introduced the concept of a "two dimensional electron gas (2DEG)", which is effectively identical to the quantum wells described previously for super lattices of Si and Ge. In the aforementioned 2DEGs, electrons are confined within a conducting (in this case Nb:STO) layer with a thickness of one unit cell. The 2DEG layers are separated by insulating dielectric layers (undoped STO). In the interlayers, the effective density of states is drastically increased, and as Seebeck coefficient is directly proportional to carrier concentration it too increases. It has been suggested that this observation can be exploited in super lattice to have a net increase in Seebeck coefficient, and thus an increase in thermopower, with the theoretical result being a ZT of 2.4 at room temperature (35) (36).

2.4 1D Nanostructuring of Oxide Materials

2.4.1 Limitations of Conventional Techniques

While thin films and bulk nanostructures are easily fabricated by a variety of techniques, the techniques used to create the 1D structures described in section *2.2.2* are limited. Electrodeposition requires a uniformly conducting material, which doped oxides when separated are not, vapor phase growth methods such as vapor liquid sold (VLS) (the technique used most commonly for Si and other intrinsic or compound semiconductors) requires a relatively low melting temperature and a satisfactory liquid catalyst. Attempts have been made to synthesize 1D oxide nanostructures directly from a vapor phase, but with mixed results (37) (38) (39) (40). Furthermore, these approaches are most commonly demonstrated with binary oxides. Complex oxides, such as STO require other approaches. Doping of oxides, which is necessary to transition oxide materials from insulators to semiconductors adds more complexity to the fabrication process. Additionally, an effective synthesis technique must have relatively high output and extremely sensitive dimension control to be effectively implemented in a device.

2.4.2 Solution Based Growth

Hydrothermal synthesis involves the decomposition of organometallic or inorganic precursors in a solution at elevated temperature. In order to obtain the desired final stoichiometry, temperature, pH, concentration and precursor formulation must be carefully controlled. Urban *et. Al.* and Joshi *et. Al.* have demonstrated that STO nanorods and nanowires can be effectively created with this approach (41) (42). While the nanowire dimensions can be less than 50 nm with lengths of many microns, these dimensions vary as a function of growth time and thus length. As growth in these scenarios is typically attributed to Ostwald ripening, a uniform distribution of the smallest diameter nanowires is unlikely. Regardless, the 1D nanostructures created with this approach are verified as crystalline by TEM and XRD, and show the desired perovskite structure and lattice constant. As these structures are fabricated in solution, testing of electrical or thermal conductivity would require drying and isolation of individual or bundles of uniform nanowires.

Another solution based technique is sol-gel processing. When allowed to dry as a bulk material, sol-gel could be considered a 3D nanostructure. Xu *et. Al.* effectively demonstrated that a sol of $La_{.95}Sr_{.05}CoO_3$ precursor could be electrospun into 35 nm fibers (43). XRD results of the technique show that the crystal structure of the electrospun fibers is identical to that of the powder used in the sol, suggesting the fibers are non-fully dense and polycrystalline. However, by measuring the thermoelectric

power output of an individual fiber, the group calculated a Seebeck coefficient that was 18% greater than that for the bulk material.

2.4.3. Template Assisted Growth

Typical template assisted uses a pre-defined "negative" structure to restrict the growth of the oxide material. Templates are typically created using lithography or anodize aluminum oxide (AAO). Following the definition of a satisfactory template, the nanostructures can be created from a vapor or liquid precursor. Bae *et. Al.* showed that an AAO template could be effectively filled using PLD (44). AAO has the advantage of regular pore sizes and spacing, in this case with a diameter of 60 nm, but must be removed after the filling the template. For this reason polymer templates are often used.

Electron beam lithography (EBL) has been demonstrated to be capable of defining sub 50 nm wide line widths, and when in conjunction with high contrast resists and developers such as poly-methyl methacrylate (PMMA) and methyl isobutyl ketone isopropyl alcohol (MIBK-IPA), features on the order of 20 nm can be formed (45) (46) (47). Polymer templates defined in this way can be used directly as deposition masks with multiple filling approaches. Regardless of filling technique, the process must take place at low temperature to avoid degradation of the resist template. Following template filling, the polymer is easily removed by organic solvents. Hydrothermal methods have been used to deposit binary oxides such as ZnO from solution into templates, forming wires and columns that show strong photolumiscent response (48) (49). Sol-gel precursors can also be used to fill templates as shown by Sun *et. Al.* using EBL and sols of $BiFeO_3$, and reaching a minimum feature size of 80 nm width for 2 micron long lines (50). When high temperature processing is required, the polymer masks can be used to make a secondary mask out of a more robust material. A metal is most commonly used for this purpose, as it can be easily etched away after use if desired. Morales *et. Al.* demonstrated a variation on this concept by first deposition an amorphous layer of STO using PLD at room temperature into a PMMA template, and then after removing the template used the amorphous STO to inhibit epitaxial growth during subsequent oxide depositions (51).

Chapter 3: Methods and Materials

3.1 Electron Beam Lithography for Substrate Patterning

Electron Beam Lithography (EBL) was used to pattern polymer resist, which was used directly as a template in the subsequent filling process. All EBL processing took place at the Center for Functional Nanomaterials, located at Brookhaven National Lab in Upton, New York. Substrates used were single crystalline (100) oriented STO, provided by CrysTec as 5x5 mm one side electromechanical polished squares. Substrates were first cleaned by rinsing in acetone, methanol, and iso-propanol in that order. Following the solvent rinse the substrates were plasma etched in an oxygen plasma asher, in a oxygen partial pressure of 100 Torr at a plasma power of 100 W for 30 seconds. Following asher processing, substrates were adhered to a silicon (Si) wafer using resist, and allowed to dry for a period of 10 minutes. The Si wafer was then loaded onto a vacuum chuck in a resist spinning apparatus. The resist used for all templates was poly methyl methacrylate (PMMA) in Anisole solvent, and abbreviated as PMMA-A. Depending on the desired final resist thickness, the weight necessary percent of PMMA in Anisole was determined using a spin-speed vs film thickness chart available from the PMMA resist manufacturer MicroChem, shown in Figure 3.1. For the templates discussed in the results section, PMMA-A4 was spun on at 3000 RPM for a final resist thickness of approximately 175 nm.

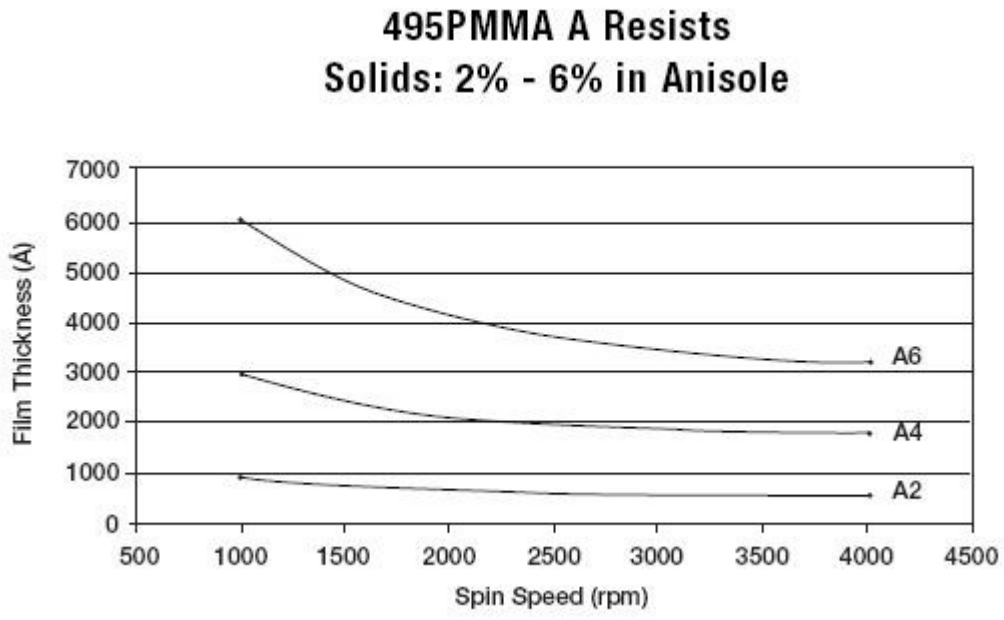

Figure 3.1 PMMA A Spin Speed Chart

After the resist is spun on to the desired thickness, the Si wafer with attached oxide substrates is baked at 180 °C for 5 minutes for drying. Once dried, the Si wafer is placed back in the resist spinner and a layer of conductive polymer is spun onto the substrates at the same spin speed as the resist. The conductive polymer used in these experiments is called ESPACER and is used to prevent charge build-up on non-conducting substrates, which leads to deflection of the electron beam during patterning. The ESPACER is also baked at 180 °C for 5 minutes.

After the PMMA and ESPACER films are dried, the substrates are inspected at a bias for imperfections, streaks, or other non-uniformities in the films. A single oxide substrate is removed from the Si wafer and loaded into the piece holder cassette of the JEOL JBX-6300FS electron beam lithography tool. Once the chamber is evacuated the substrate can be patterned. Patterns were designed using the computer aided design (CAD) software LayoutEditor. The nominal line width, period and total pattern area are defined at this stage. Templates were designed according to desired functionality. For nanowires, horizontal trenches were created. For nanodots or "pegs" for mock thermoelectric devices, boxes were created. Figure 3.2 shows a design schematic for both cases, in which D represents diameter, P is pitch and L is the length of the trench or total array.

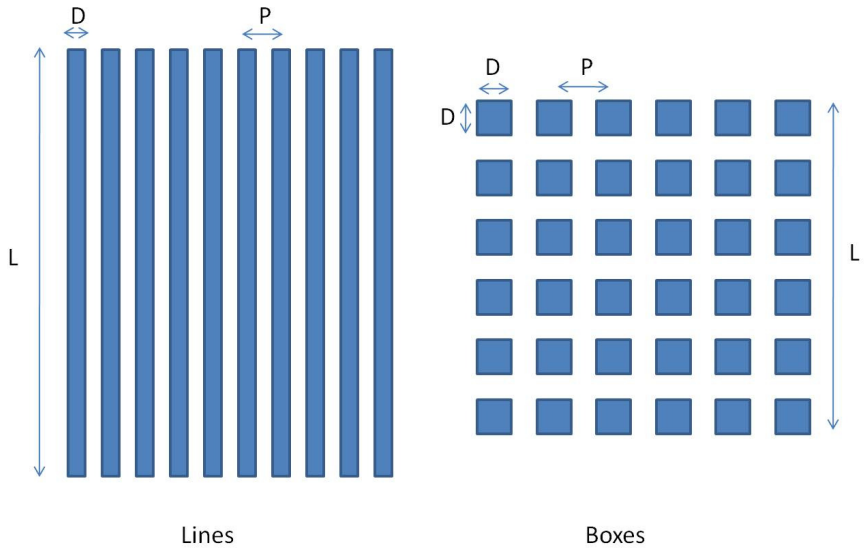

Figure 3.2 Template Design Schematic

The values of D and P varied between samples, which a minimum design value of 10 nm for D and 100 nm for P. L was held at a constant 500 µm, except for one sample in which L was equal to 2 mm. Individual substrates were patterned with nine 500 x 500 µm arrays in a 3 x 3 orientation. Once a pattern

is designed, it is converted to the JEOL compatible format using Layout Beamer. The desired dose of electrons for the pattern is also determined at this time using the following equation.

$$Dose = \frac{current \times time}{area} = \frac{t_{min}}{pixels^2 \times current} \qquad Eq. 7$$

In the above equation, the dwell time t_{min} must be satisfied for a given pixel density, current, and final desired dose. The minimum dwell time is defined by the electron beam tool, and in this case is 20 ns. The Layout Beamer file is then compiled on the JEOL control terminal and is ready for use. Before every exposure, the JEOL JBX-6300FS must be calibrated in accordance with the Center for Functional Nanomaterials standard operating procedure. Calibration consists of selecting a calibration table designed for the working current. For all exposures the working current, and thus the calibration table used was 4 nA. During calibration, the position, shape and current density of the electron beam are optimized for exposure. In addition to the 4 nA current, all exposures used an accerlating voltage of 100 keV and electrons are generated from a ZnO/W thermionic electron gun. At this point the substrate can be patterned with the designated CAD design. Patterning takes between 10-20 minutes depending on the pattern size and feature density. Following exposure, the PMMA resist is placed into a developer solution. PMMA based resists are developed in a solution of Methly iso-butyl Ketone and iso-propanol for 1 minute, and then placed into pure isopropanol to end the developing process. PMMA is a positive resist, meaning only the areas exposure to the electron beam will be removed during developing.

3.2 Pulsed Laser Deposition for Template Filling and Film Deposition

Pulse Laser Deposition (PLD) was used in this work for the fabrication of thin films and to fill the PMMA templates created as described in the previous section. A KrF Excimer laser with a wavelength of 248 nm was used as the ablation source in these materials. The Excimer laser functions by energizing the Excimer premix gas (KrF with an inert buffer) with a high voltage which creates a short lived dimer species from the premix gas. When the dimer decomposes, the characteristic wavelength light is released. The laser light is then directed through a focusing lens with adjustable position and onto an ablation target inside of a vacuum chamber. Typical base pressure for ablation is in the high vacuum range, or about 10^{-6} Torr. During ablation, the target can be rastered and rotated for even ablation. Ablation creates a plume of plasma and vapor which is released orthogonally from the surface of the target. This plume is directed onto a substrate, which is typically heated and crystalline. Gasses can be added to the vacuum chamber to control growth characteristics and serve as reactants with the plume. A schematic of the PLD apparatus is provided in Figure 3.3.

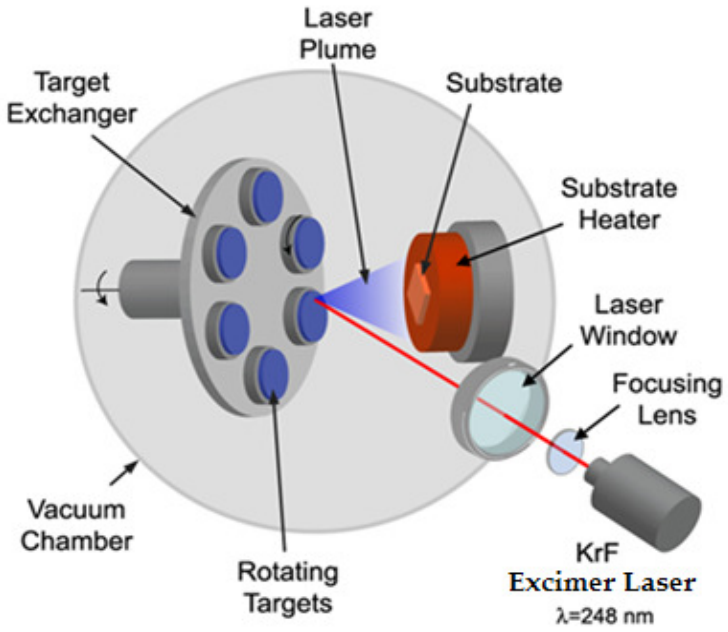

Figure 3.3 The PLD Apparatus

Premix pressure is held around 2350 Torr in the laser chamber, and the voltage source is fixed at 25 kV. Before each ablation, the laser energy is measured via an Orion hand held photo detector. If the laser energy is within an acceptable range (150 to 200 mJ) the experiment can proceed. Otherwise the premix gas is replaced via an automated refilling procedure. After measuring the laser energy, the energy density can be calculated using the following equation.

$$Energy\ Density = \frac{Laser\ Energy\ (J)}{Spot\ Size\ (cm^2)} \qquad Eq.8$$

Spot size is measured directly using laser paper. The position of the focusing lens is adjusted to set the desired energy density for the measured laser energy. Laser repetition rate can also be specified. For a given set of experimental parameters (laser energy density, repetition rate, chamber pressure and substrate temperature) a step sample is made via masking technique. The step height is then measured with a profilometer to determine growth rate. In this way, a desired film thickness can be selected by choosing the corresponding number of laser pulses.

Prior to all PLD experiments, the chamber is cleaned with acetone and laboratory grade tissue paper. Blank (un-patterned) substrates are prepared by sonication of the substrate in a bath of acetone and then iso-propanol for 5 minutes each. The substrates are then dried under flowing nitrogen and placed on

the substrate heater using silver paint. Ablation targets are mounted onto target holders using silver glue, and sanded between depositions to prevent the formation of a dimple. Once the target and substrate are mounted in the vacuum chamber, a turbo molecular pump with a rotary vane backing pump is used to draw high vacuum. Once under vacuum, the targets are pre-ablated with 2000 pulses of the laser at a frequency of 10 Hz to remove oxides or other contaminates from the target surface. During pre-ablation the substrate is covered by a moveable shield. Process conditions vary for the desired final product however factors such as film roughness, crystallographic orientation, or physical properties are the typical factors to optimize in the deposited film. Films were deposited directly onto the cleaned substrates at elevated temperature, either in high vacuum or a reaction gas. Templates were filled at room temperature followed by a liftoff process.

The template liftoff process was used to remove deposited material from the substrate in all areas except by those patterned via EBL. Substrates with PMMA templates were mounted directly on the heater in the PLD chamber without cleaning, as the solvents used during this step would remove the template. Following deposition, the substrates were placed into a small beaker containing 10 mL of acetone, heated on a hot plate to a temperature of 90 °C for 10 minutes. At this point the deposited material on the non-patterned regions of the PMMA template are visibly warped and cracked. The beaker is then sonicated for approximately 10 seconds by hand to remove this part of the template. Following the liftoff procedure, freestanding features are left on the substrate which can then be subjected to annealing or directly analyzed.

3.3 Scanning Electron Microscopy

Scanning Electron Microscopy (SEM) was used to characterize both PMMA templates and the resulting features after PLD. Two SEMs were used for this project. First, a Hitachi S-4800 UHR FE-SEM located at Brookhaven National Lab was used for direct inspection of the PMMA templates while developing the exposure parameters. For use in this SEM, samples had to be coated with approximately 5 nm of an Au-Pt film via a tabletop sputtering machine. This prevented charge buildup on the insulating samples during observation. The second SEM used was a FEI Quanta 600 FEG environmental SEM. The environmental aspect allowed observation of the insulating samples without coating by introducing a partial pressure of water vapor into the SEM chamber. In this way, templates could be analyzed before and after PLD. Accelerating voltage, spot size, and chamber pressure for the environmental SEM were manipulated for optimum imaging.

3.4 Optical Microscopy

An Olympus BX51 optical microscope was used for inspection of PMMA templates before exposure and after developing. This provided qualitative information regarding uniformity of the spun on resist and check for delaminating after developing.

3.5 Atomic Force Microscopy

Atomic Force Microscopy (AFM) was used to compliment SEM during morphology characterization of PMMA templates, patterned arrays and films. In addition to the lateral morphology information provided by SEM, AFM is capable of reporting surface roughness as well as height. A Veeco MultiMode AFM was used. The AFM was operated in contact mode with Si probes. Figure 3.4 provides a schematic of contact mode AFM operation (52).

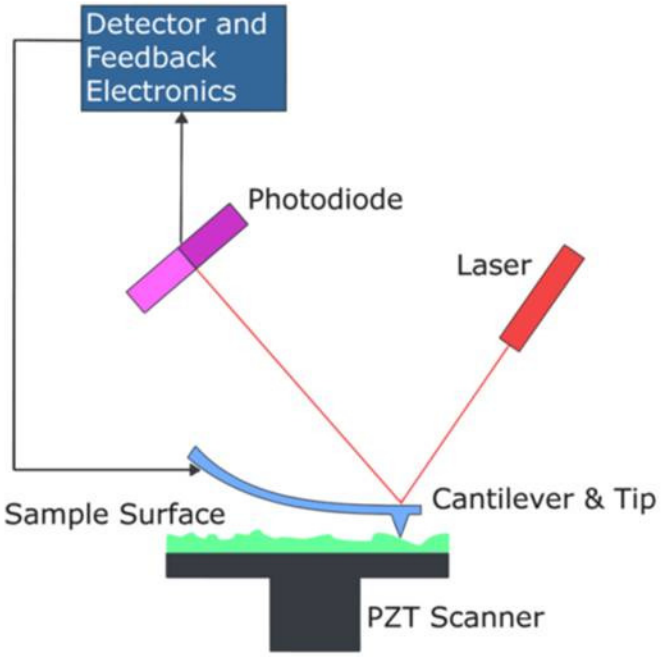

Figure 3.4 AFM Operated in Contact Mode

AFM samples were mounted onto a sample holder with two sided tape and placed under a head containing the laser, photo diode and cantilever. Using an optical microscope, the laser is first positioned on the tip of the cantilever to maximize the reflected laser intensity. Motors are used to lower the piezoelectric sample mount into proximity with the tip, at which point the recorded cantilever deflection from the photodiode is zeroed. The piezoelectric actuator is then used to bring the sample surface into

direct contact with the AFM tip. The raster speed used for all AFM samples was 2 Hz with a scan width of 5 μm.

3.6 X-ray Diffraction

X-ray diffraction (XRD) was performed using a Phillips Xpert Pro powder diffraction XRD. Samples were mounted using modeling clay and manually centered and rotated for maximum diffraction intensity. X-ray analysis allowed for crystallographic analysis of films, which were used as an analog for the patterned substrates. The Bragg relation, shown below, was used to calculate lattice spacing.

$$n\lambda = 2dsin\theta \qquad Eq.9$$

Where λ is the wavelength of the interrogating x-rays, which for Cu Kα is 1.5419 Å. The measured angle of diffraction θ is the output of the XRD experiment, and is used in the Bragg equation to solve for d, the lattice spacing. Changes in lattice spacing and relative intensity of diffraction peaks are used to determine extent of crystallization and changes in composition or morphology. The Scherrer equation can be used to calculate average grain size in the sample.

$$\tau = \frac{K\lambda}{\beta cos\theta} \qquad Eq.10$$

As for the Bragg relation, the Scherrer equation is dependent on x-ray wavelength and diffraction angle. The full width at half of the maximum intensity β in radians is used for a given diffraction angle to determine average grain size. K is a shape factor assumed to be 0.9 for spherical grains.

3.7 X-ray Photoelectron Spectroscopy

X-ray Photoelectron Spectroscopy (XPS) was used to analyze sample composition. A PHI Quantera SXM was used to take sputter depth profiles in both films and patterned arrays. XPS use x-rays to bombard a sample which release photon-stimulated electrons, or simply photoelectrons. These photoelectrons have characteristic energies dependant on the bond which was broken to free them, and can be used to determined relative composition percentages for individual elements in a sample in addition to bonding state between elements for high resolution scans with very narrow pass energies. XPS is an extremely surface sensitive technique, sampling only the top few nanometers of the sample, but has a large interrogation area on the order of 20 μm^2. Depth profiles have the added benefit of revealing information about diffusion and film uniformity. As x-ray photos are used rather than electrons (as in

EDS or Auger spectroscopy) insulating samples can be analyzed. Low resolution scans were used in this report, and thus only elemental concentrations and no bonding information is provided.

3.8 Electrical Conductivity

A Keithley 4200 SCS van der Pauw sheet resistance measurement system was used to measure electrical conductivity of film samples. Films are most commonly measured using a 4-point collinear setup, however this method is extremely sensitive to sample size and probe placement. As the films in this project were on 5 x 5 mm substrates, the necessary geometric arrangement for accurately measuring electrical conductivity with the collinear technique was impossible. The van der Pauw method also uses 4 contact probes, however their arrangement is arbitrary. Instead, the sheet resistance is calculated by alternating an applied current to two probes at a time and measuring the voltage potential from the other two. The current is supplied to different combinations of probes and the resulting voltages are used to calculate the resistivity. In total, 8 combinations of the probes are used to measure voltage. Figure 3.5 shows a conventional arrangement for these measurements (53).

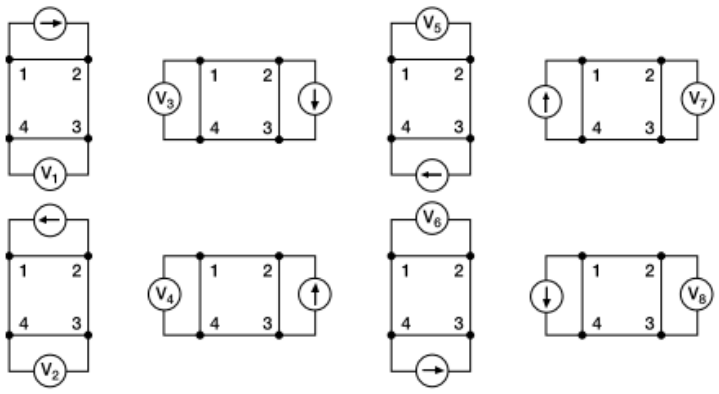

Figure 3.5 Voltage Measurements using the van der Pauw Method

Equations 10 and 11 are then used with the measured voltages to calculate the volume resistivity in Ω-cm, which are then averaged as shown in equation 12 for the overall sheet resistance.

$$\rho_A = \frac{\pi}{ln2} f_A t_s \frac{(V_1 - V_2 + V_3 - V_4)}{4I} \qquad Eq.11$$

$$\rho_B = \frac{\pi}{ln2} f_B t_s \frac{(V_5 - V_6 + V_7 - V_8)}{4I} \qquad Eq.12$$

$$\rho_{AVG} = \frac{\rho_A + \rho_B}{2} \qquad Eq.13$$

In equations 10 and 11, t_s is the sample thickness in cm, and $f_A$and f_B are geometrical relationships related to the resistance ratios Q_A and Q_B defined as follows.

$$Q_A = \frac{V_1 - V_2}{V_3 - V_4} \qquad Eq.14$$

$$Q_B = \frac{V_5 - V_6}{V_7 - V_8} \qquad Eq.15$$

The values for f_A and $f_B$are solved by plotting the following relationship with their respective Q values.

$$\frac{Q+1}{Q-1} = \frac{f}{0.693} arc\cosh\left(\frac{e^{0.693/f}}{2}\right) \qquad Eq.16$$

Chapter 4: Results and Discussion

4.1 Template Fabrication using EBL

Several template design values were implemented in accordance with the dimensions depicted in Figure 3.2. The templates used in this section are detailed in Table 4.1.

Table 4.1 Templates used for Characterization

Template #	Nominal Dimension	Dose (uC/cm2)	Figure #
1	100 nm lines and spaces, 500 um length	400 to 1040 by 80 (3x3)	4.1
2	100 nm lines and spaces, 1 um length	400 to 1040 by 80 (3x3)	4.2, 4.6
3	100 nm, 250 nm, 500 nm and 1 um lines and spaces, 500 um length	800	4.3
4	1 um lines and spaces, 500 um length	720 to 780 by 20 (2x2)	4.4
5	1 um lines and spaces, 500 um length	780	4.4
6	50 nm lines, 1 um spaces, 500 um length	1040 to 1680 by 80 (3x3)	4.6
7	10 nm, 30 nm, 50 nm and 100 nm lines, 1 um spaces, 500 um length	780	4.6
8	10 nm, 30 nm, 50 nm and 100 nm lines, 1 um spaces, 500 um length	1400	4.7
9	50 nm lines, 1 um spaces, 500 um length	2000 to 5200 by 800	4.8
10	10 nm, 30 nm, 50 nm and 100 nm lines, 1 um spaces, 500 um length	5200	4.9
11	50 nm lines, 1 um space, 500 length	4000 to 5600 by 250	4.1
12	10, 20, 30, 50, 75 and 100 nm lines, 50, 100, 500 nm boxes	5200	4.13,4.14

Initial tests for template exposure resulted in unresolved patterns. Exposed areas of resist resulted in partially or completely delaminated features after developing. This effect was observed for all templates with a pitch of 100 nm or below, and did not reveal a dependence on dose. Some representative images taken in optical microscopy are shown in Figure 4.1.

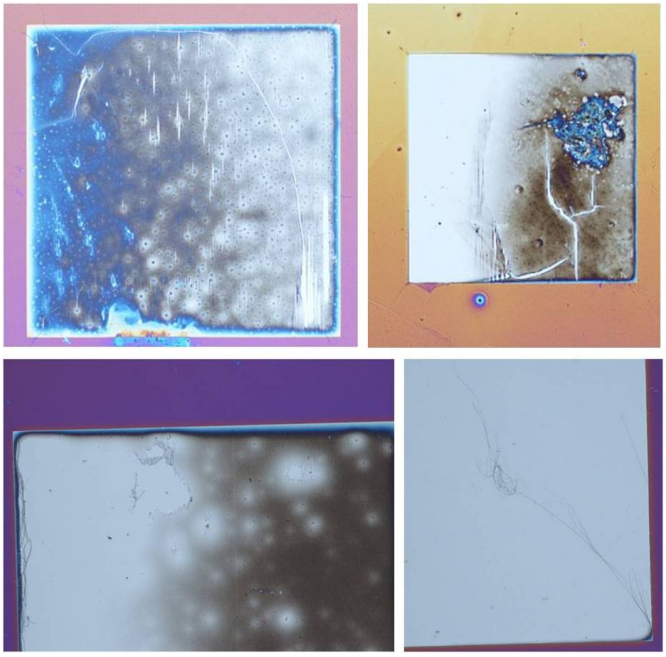

Figure 4.1 Optical Microscopy Images of Template 1

As the lines 500 μm in length were broken, the effect of shortening the line length while maintaining the original pitch and critical dimension was considered. A pattern was designed with 1 μm line length and the original values for diameter and pitch, template 2. Figure 4.2 shows the optical microscopy results from this test.

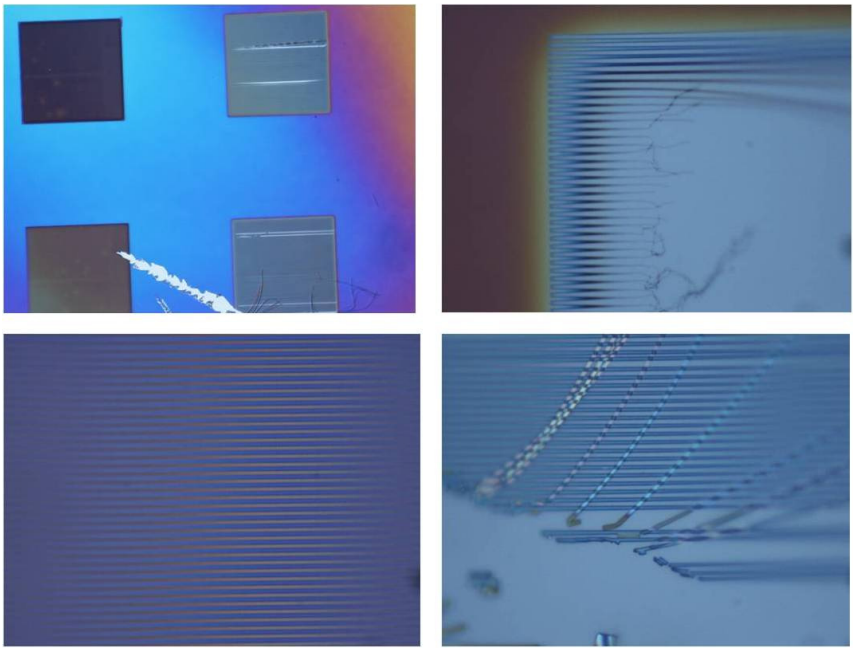

Figure 4.2 Optical Microscopy Images of Template 2

Template 2 did reveal some sensitivity to dose, and at a value of 780 μC/cm^2 the features were resolved without delaminating. From these results, it was concluded that proximity dosing was responsible for the delamination of the100 nm pitch samples, rather than the length of individual wires. Template 3 was designed to test this conclusion, and included the previously tested 100 nm lines and spaces, 250 nm lines and spaces, 500 nm lines and spaces and 1 μm lines and spaces. Only the 1 μm lines and spaces element in the 2x2 array was resolved at 780 μC/cm^2, shown in Figure 4.3. All other regions were completely delaminated during developing.

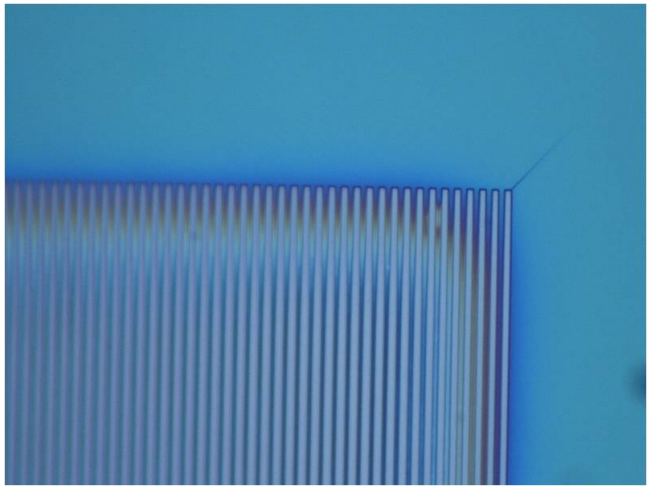

Figure 4.3 Optical Microscopy Images of Template 3

It is apparent that in the center of the exposed region shown in Figure 4.3, the open spaces become significantly broadened. This evidence supports the previously stated conclusion regarding proximity dosing. The results from template 3 were recreated for ESEM analysis, as well as for the subsequent filling experiments. ESEM analysis of template 4, which was exposed between a range of 720 to 780 μC/cm^2 revealed that the spaces were not completely cleared of resist at the lowest dose used, commonly referred to as "scumming" in the semiconductor industry. At the higher dose, which was used for template 5, the spaces are found to be completely cleared. In both cases however, the pattern broadening that was observed in optical lithography can be seen, with maximum effect occurring at the center of the patterned area. ESEM images of templates 4 and 5 are shown in Figure 4.4.

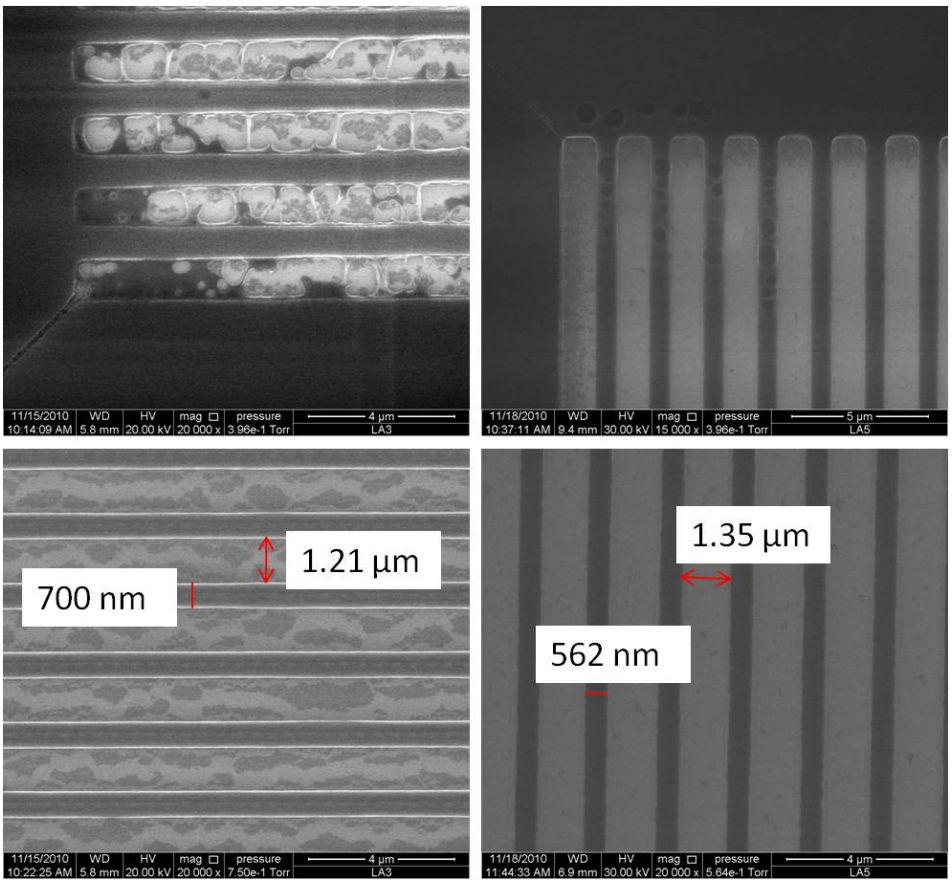

Figure 4.4 ESEM Images of Templates 4 and 5

The 1 µm length, 100 nm line and space pattern (template 3) was also investigated using ESEM. Broadening of the trench here was less severe, showing an average space size of about 110-120 nm and line size of 80-90 nm, shown in Figure 4.5, possibly due to a reduced feature density.

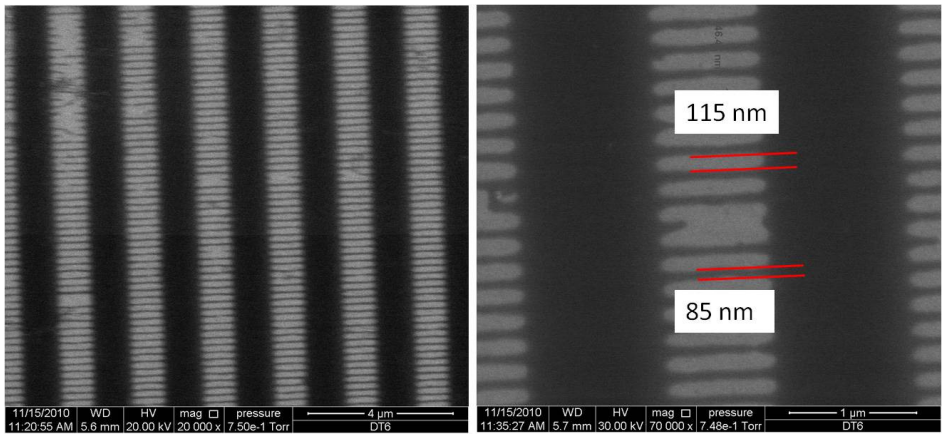

Figure 4.5 ESEM Images of Template 2

In an effort to reduce the negative effects of proximity dosing observed in samples 1 and 2, templates were designed with 100 nm spaces and below, but with a pitch held at 1 μm. Patterns of this design exposed in the same range as the larger width patterns (780 μC/cm^2) showed incomplete line definition, characterized by scumming and bridging between line walls. Figure 4.6 shows SEM images of templates coated with Au/Pt at a dose of 780 and 1680 μC/cm^2 (templates 7 and 6 respectively). Nominal line width was 50 nm. The inset of the 1680 μC/cm^2 image shows the bridged spaces at a higher magnification.

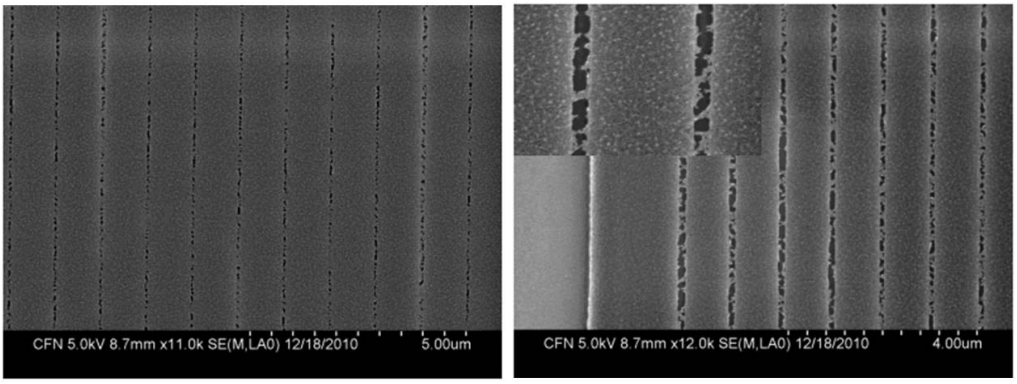

Figure 4.6 SEM images of 50 nm lines exposed at 780 (left) and 1680 (right) μC/cm^2

For varying nominal line widths, the same morphology was observed at similar dose values. Figure 4.7 shows nominally 30 nm and 100 nm lines exposed at 1400 μC/cm^2 with significant bridging and scumming, the combination of these effects leaving the 30 nm spaces almost completely closed.

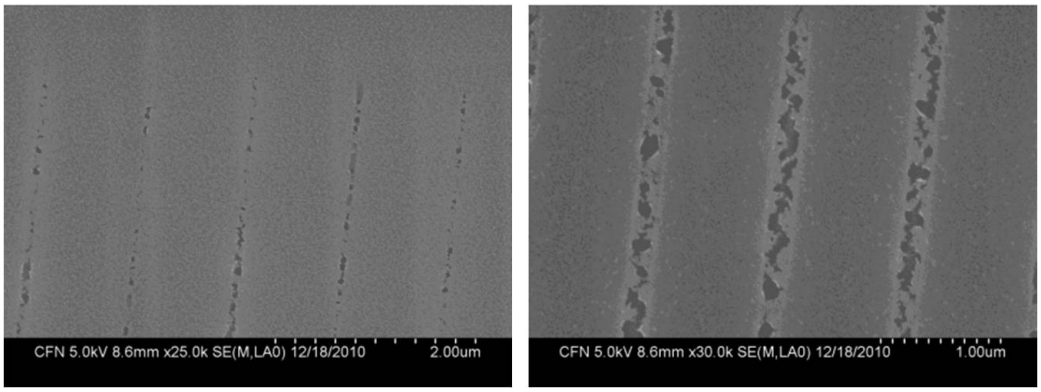

Figure 4.7 SEM images of 30 nm (left) and 100 nm (right) spaces exposed at 1400 μC/cm^2

Dose values were increased for the 50 nm space, 1 μm pitch pattern until completely cleared lines were obtained. While above 2000 μC/cm^2, complete bridging of the spaces was largely unobserved, rough space edges were still apparent. At 5200 μC/cm^2, smooth edged and fully cleared lines were achieved

however the final measured diameter was roughly 180 to 200 nm – a 4x increase over the original value, shown in Figure 4.8.

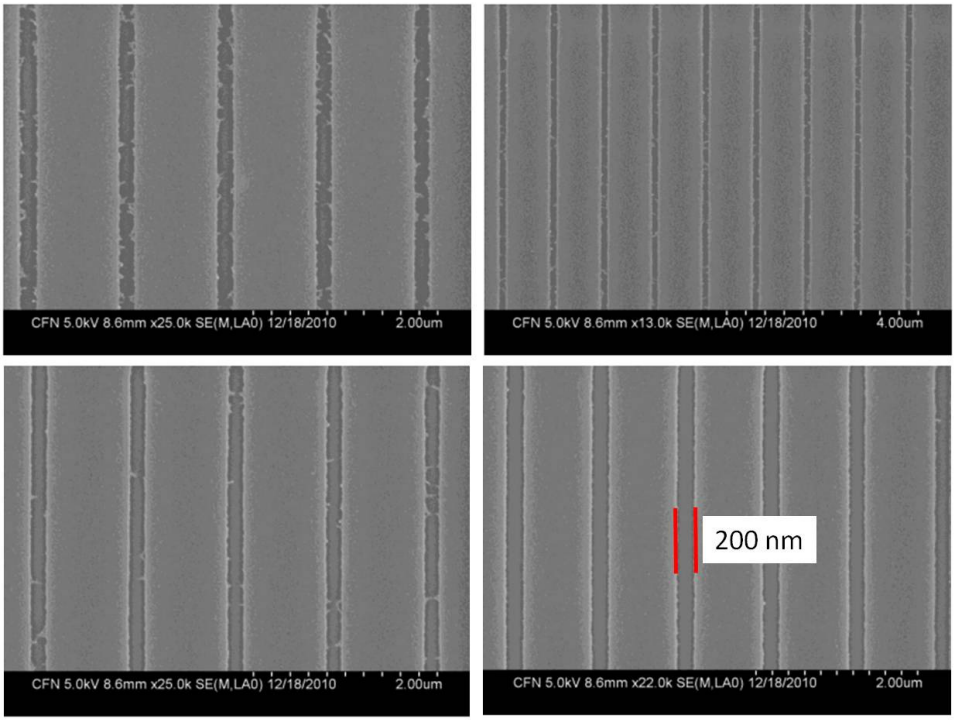

Figure 4.8 SEM images of 50 nm lines at various doses: clockwise from top 2000, 3600, 4000 and 5200 μC/cm^2

All templates showed significant broadening over nominal dimensions, the degree of which increasing at smaller sizes. While to some extent this was an actual occurrence, line broadening became exaggerated during SEM observation. Figure 4.9 shows 10 nm lines exposed at 5200 μC/cm^2. Line broadening due to the SEM electron beam is clearly visible, causing an increased space diameter of over 50%. Line broadening could be avoided if samples were observed only in low magnification.

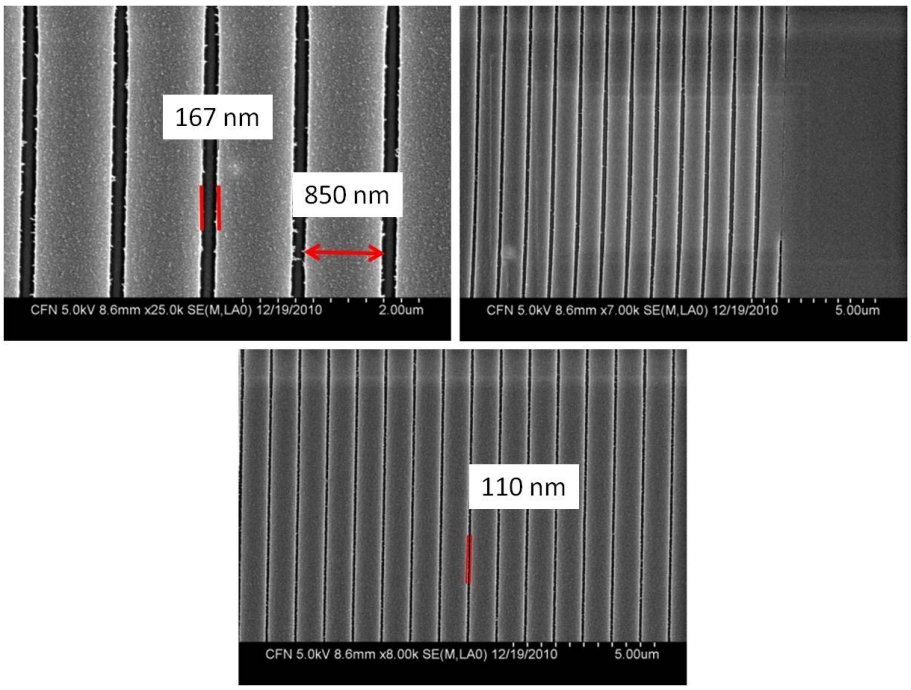

Figure 4.9 SEM images showing line broadening in 10 nm Template

To avoid line broadening, AFM was also used to inspect unfilled templates. Figure 4.10 shows nominally 50 nm lines developed at 4600 μC/cm^2, with a resulting actual dimension of roughly 200 nm, which agrees with the SEM measurement. AFM analysis of the templates showed that the template walls were sloped. This is to some extent due to the AFM probe, however this sloping is also observed after the templates are filled.

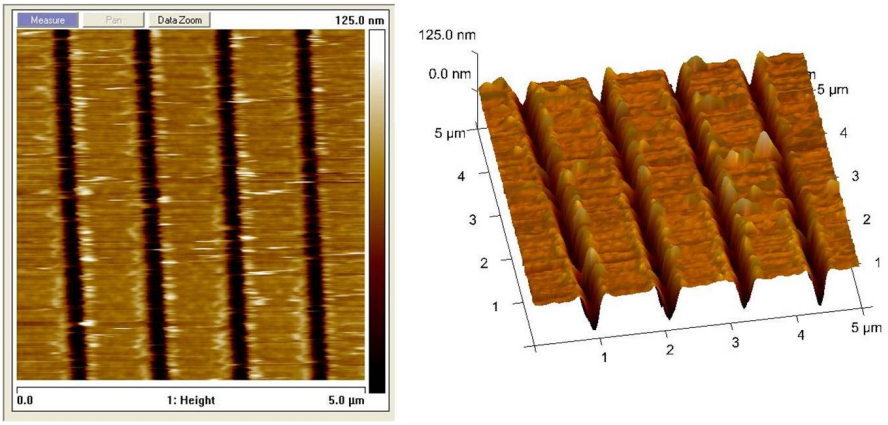

Figure 4.10 AFM image of 50 nm template exposed at 4600 μC/cm^2

4.2 Template Filling using PLD

After analysis, several templates were selected to be filled using PLD by ablating a $SrTi_{.8}Nb_{.2}O_3$ target. The number of laser pulses was varied to control the thickness of the deposited material, and in theory the height of the nanostructures. Annealing was also tested, both before and after the liftoff procedure. All templates were filled under high vacuum (10^{-6} Torr) at room temperature with an energy density of 2 J/cm^2 and a repetition rate of 5 Hz.

Initial filling parameters were based on a growth rate assumption taken from profilometer measurements. At an assumed growth rate of .24 Å per laser pulse, 4167 pulses would result in a film of roughly 100 nm. However, this deposition resulted in overfilling of the 1 µm line and space templates. Overfilling was minimal towards the edges of each patterned area, but was nearly uniform in the center of the patterned areas, where the filled areas were closest together due to the overdosing effect described in the previous section. Figure 4.11 shows overfilling of template 5. Deposited material appears as the lighter gray lines at the bottom of the left image in Figure 4.11. On the right side, the overfilled material is visible as the brighter areas between the deposited lines.

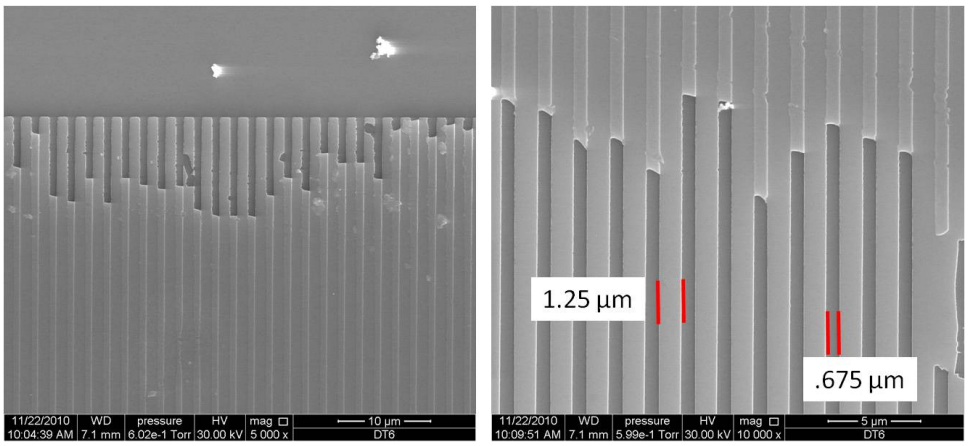

Figure 4.11 ESEM Images of Overfilled Templates

Template 2 which had nominally 100 nm lines and spaces of 1 µm in length, and template 4 which had 1 µm lines and spaces where scumming was observed at the lower doses used were also filled with the nominally 100 nm of $SrTi_{.8}Nb_{.2}O_3$. Figure 4.12 shows these results.

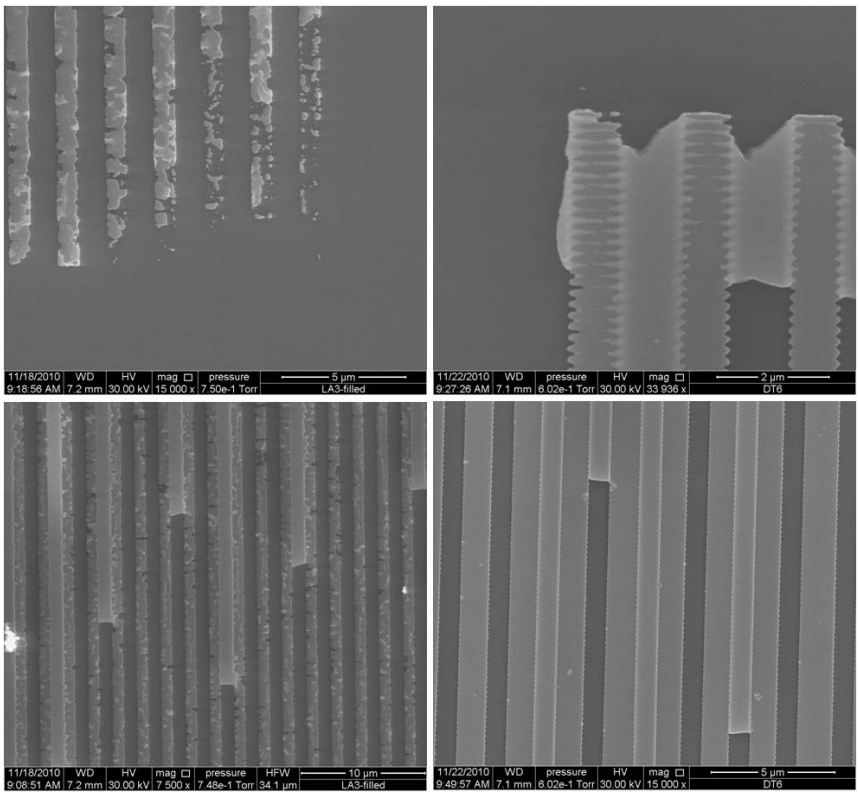

Figure 4.12 ESEM Images of filled Templates 4 (right side) and 2 (left side)

Template 4 shows both overfilling and a generally rougher morphology that that of the filled template 5. Lines appear broken and mottled, most likely due to damage incurred during the liftoff procedure of deposited material on top of the remaining resist in scummed areas. Figure 2 shows that while the templates themselves had regions of cleared resist, the applied PLD and liftoff technique is unable to resolve such a small pitch. Instead, the features have become fused together. In the top right image taken near the corner of an exposed region, the pitch is maximized as overdosing is minimized, and thus the resulting structures after filling are visible. In the lower right hand image, the exposed areas are completely fused, resulting in a rippled structure with a 1 µm width. After reducing the number of pulses by half, overfilling was no longer observed. Annealing of the filled template was also tested immediately after deposition, but before liftoff, which resulted in the formation of a partially formed film shell which was not removable during liftoff. Images of under filled and annealed templates are shown in Appendix A.

Templates 9 through 11 were all filled with either 2000 or 3125 pulses roughly equal to 48 and 75 nm thickness respectively based on profilometer measurements of films deposited on partially masked substrates. Overfilling was not observed for any of line and space patterns in these samples. Furthermore, above a dose of 5200 µC/cm^2, no obvious changes to morphology were observed. Figure 4.13 and 4.14

show template 12, not pictured in the template morphology section, which was exposed at a dose of 5200 $\mu C/cm^2$. Template 12 had 10, 20, 30, 50, 75 and 100 nm lines at a pitch of 1 µm, as well as 50, 100 and 500 nm boxes at a pitch of 500 nm, 1 µm and 1 µm respectively. Deposited with 2000 pulses no overfilling was observed with the exception of the 500 nm boxes, which were partially merged as shown in figure 4.15. All images shown in Figures 4.13 and 4.14 were taken after Au/Pt coating in a high vacuum SEM with an 8.1 mm working distance at a magnification of 25 K, corresponding to a 10.2 µm horizontal field width. The nominal line diameter is displayed in the upper left hand corner along with the actual dimensions within noted within the image. The SEM image in figure 4.15 was taken with an environmental SEM.

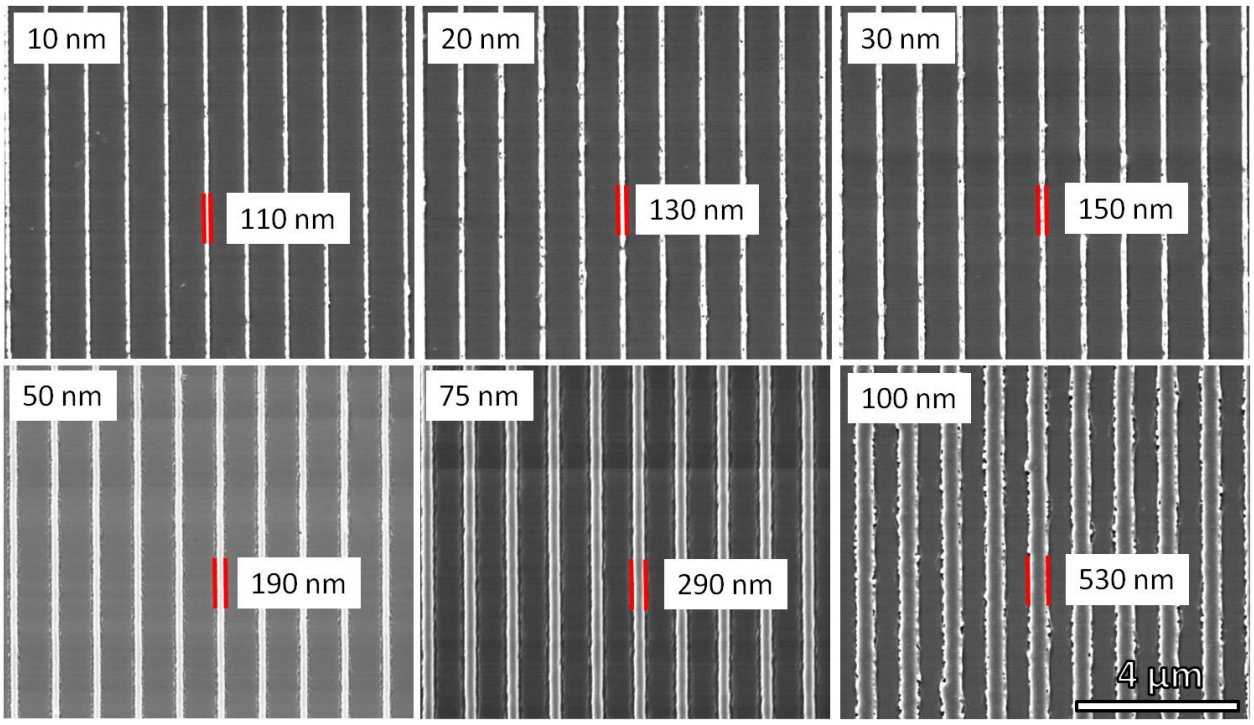

Figure 4.13 SEM Images of Filled Template 12 - Lines

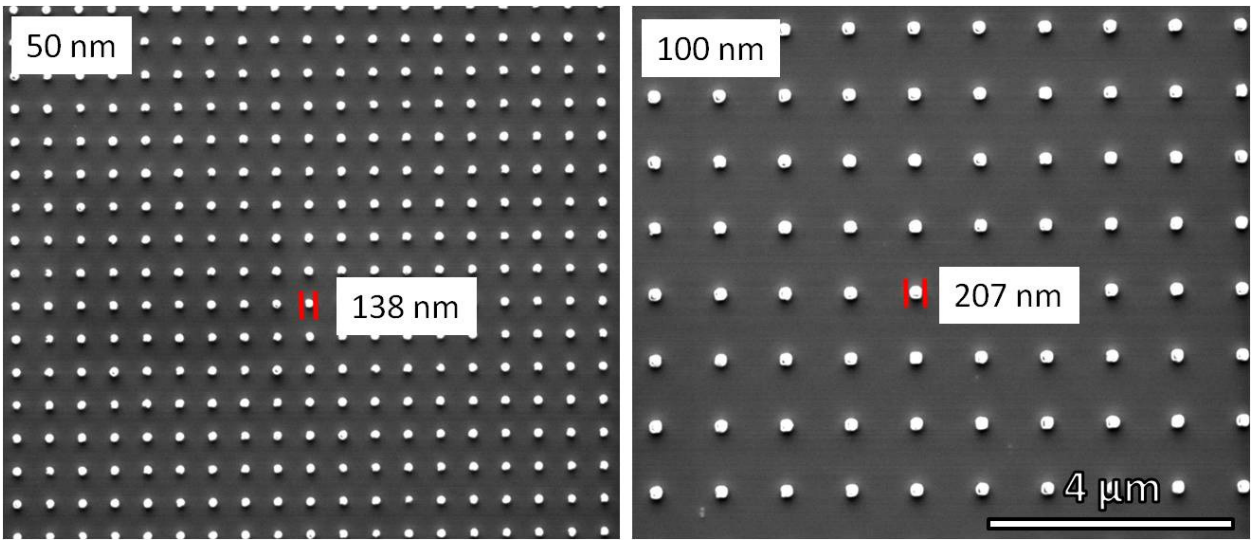

Figure 4.14 SEM Images of Filled Template 12 – 50 and 100 nm Boxes

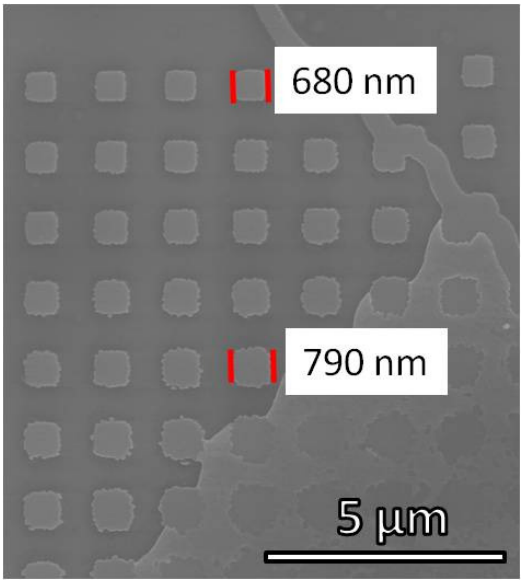

Figure 4.15 E-SEM Images of Filled Template 12 – 500 nm Boxes

While the results from template 12 represent the smallest features so far produced with this method, three observations can be made. First, at a dose of 5200 µC/cm^2, features of less than 100 nm cannot be resolved at this pitch, though perhaps it may be possible for boxes of a 10 nm nominal dimension. Second, that at a constant dose, the expansion of observed versus nominal dimension has a nonlinear dependence on feature size which is depicted graphically in Figure 4.16. The third observation is that the edge quality is severely reduced with increasing feature size for the same dose, as seen in the rough edges of the larger lines. This can be seen in both figures 4.13 and 4.15.

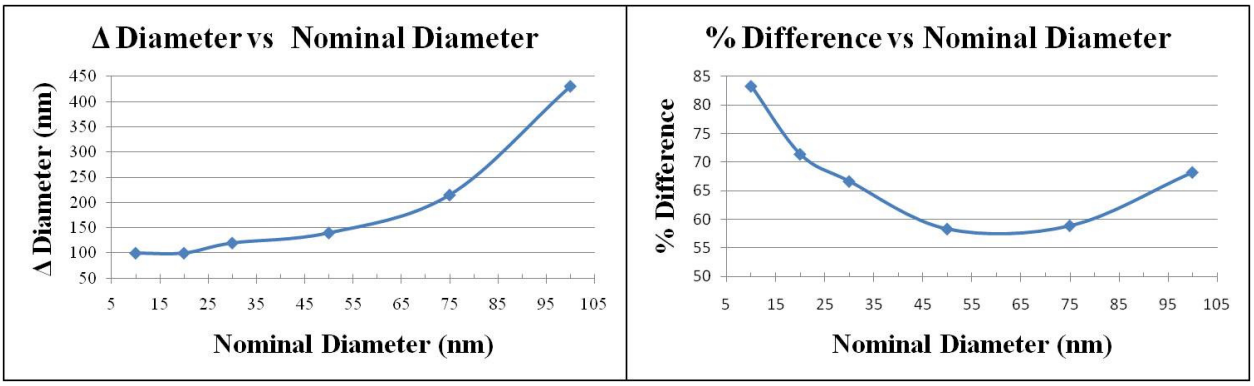

Figure 4.16 Measured vs Nominal Diameter for Filled Templates

AFM measurements of the same line structures depicted in Figure 4.13 reveal an average height of 150 nm; three times that of the assumed height based on growth rate measurements. This explains the overfilling observed in the 1μm samples. The templates were actually being filled with about 300 nm of $SrTi_{.8}Nb_{.2}O_3$, which greatly exceeds the nominal 175 nm resist thickness. Furthermore, AFM studies showed that while at the largest line widths the edge roughness increases and the topside roughness decreases with increasing thickness, shown in Figure 4.17. Actual dimension as it was calculated in the SEM images from figure 4.13 is shown to the bottom left of each AFM image.

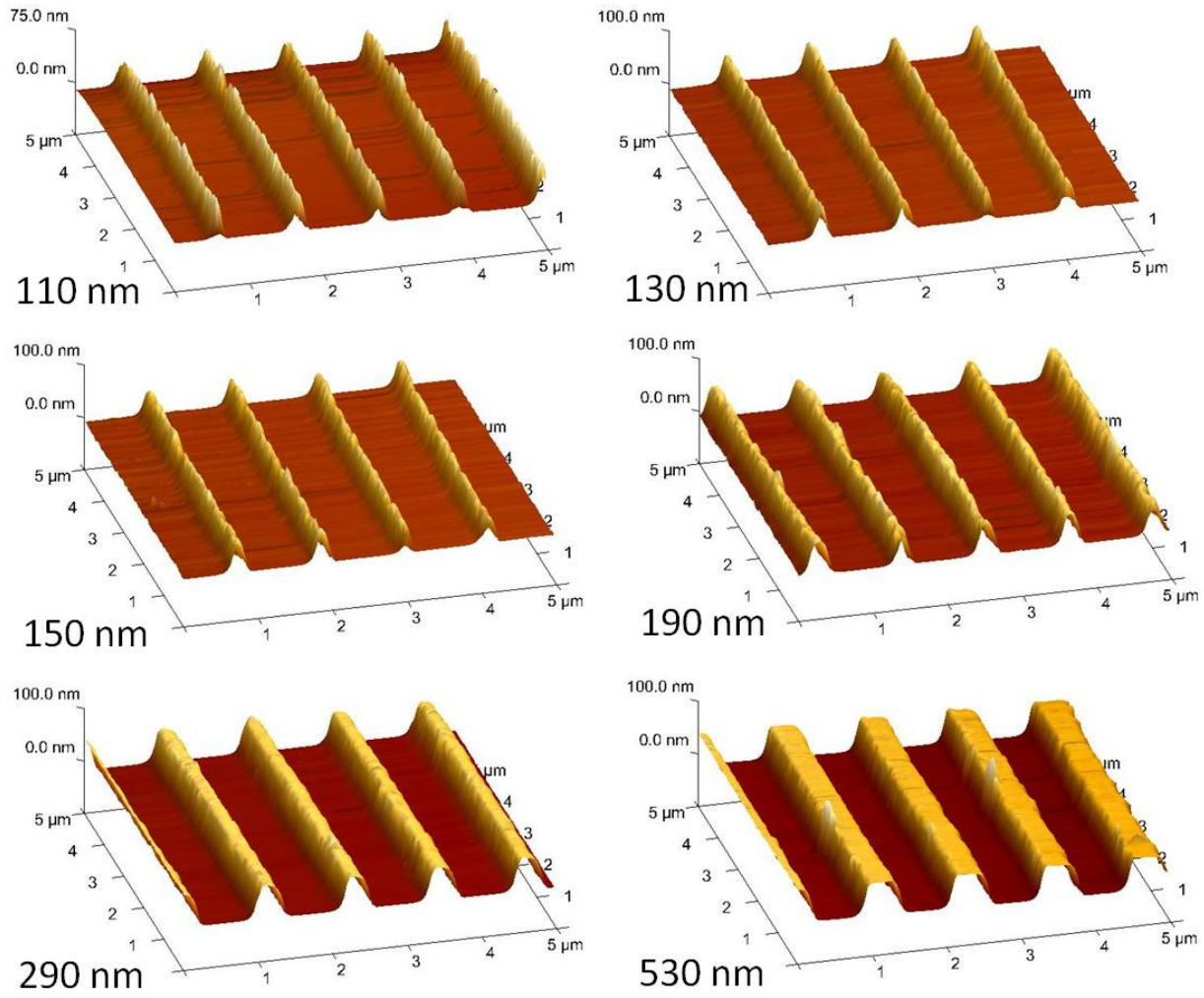

Figure 4.17 AFM Images of Filled Template 12

4.3 Discussion

Electron beam lithography was used to pattern PMMA resists on STO substrates. While the minimum feature width as defined by the EBL design software was 10 nm, the minimum observed feature width was on the order of 100 nm. Furthermore, features of high density resulted in severe overdosing while the smallest sparsely packed features required a massive dose when compared to the larger features.

Overdosing in EBL is commonly explained by means of the proximity effect. In brief, the accelerated electrons which are used to expose the resist layer are not confined to the volume directly beneath the exposed area. The electron interaction volume is well characterized for materials such as Si, and is strongly affected by the incident energy of the electrons (acceleration voltage) and the atomic

number of the material being irradiated. In general, higher accelerating voltages lead to a deeper penetration depth while higher atomic number leads to a shallower one. A graphical depiction of this relationship is shown in Figure 4.18.

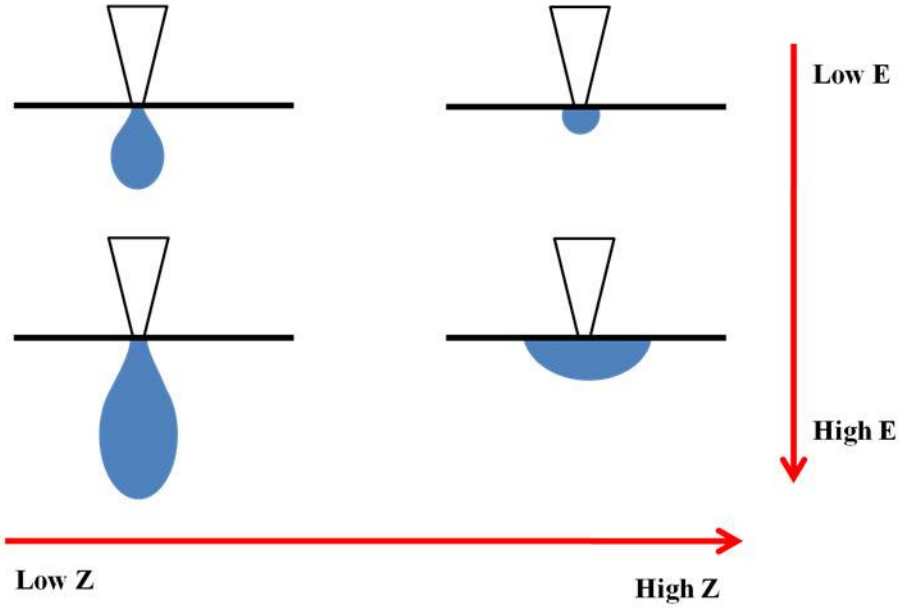

Figure 4.18 Electron Interaction Volumes

The electron interaction volume describes the motion of all electrons produced from the incident beam. The maximum theoretical range R for an electron entering a sample can be described as a function of the atomic weight A in grams/mol, incident electron energy E in keV, atomic number Z and density ρ in grams/cm^3. Equation 16 shows this relationship.

$$R(\mu m) = \frac{0.276 \times A \times E^{1.67}}{Z^{.89} \times \rho} \qquad (Eq.17)$$

For a compound material such as STO, A is assumed to be the sum of the atomic weights divided by the total number of atoms per molecule, and Z is defined as the effective atomic number Z_{eff} shown in equation 17.

$$Z_{eff} = \sqrt[2.94]{f_a(Z_a)^{2.94} + f_b(Z_b)^{2.94} + f_c(Z_c)^{2.94} \ldots . + f_n(Z_n)^{2.94}} \qquad (Eq.18)$$

Where f_n is defined as the fraction of total electrons (Z_n/Z_{total}) in the compound, and Z_n is the atomic number for the given element. For the STO substrates used in this project Z_{eff} is calculated to be approximately 30, A is 36.697 g/mol, ρ as provided by the substrate manufacturer is 5.12 g/cm^3 and E is 100 keV, resulting in a range of 20.86 μm. Secondary electrons which are produced near the surface of

the interaction volume travel the farthest distance in the sample, possibly approaching the theoretical range, but are of low energy and therefore have minimal contribution to proximity dosing. Backscattered electrons are produced when the incident electrons are redirected by the atomic nuclei of the substrate/resist, and maintain a large portion of the incident energy. For this reason they are problematic and can result in significant proximity dosing. In Si, backscattered electrons have been shown to travel up to 31 μm with 74% of the incident energy (54).

Ideally, electrons are driven deep into the substrate by the high accelerating energy used in electron beam lithography to avoid localized backscattering. However, as the atomic number of STO is significantly greater than that of Si (Z_{eff} of 30.2 vs Z of 14 for Si), backscattering can be considered significant. The observed overdosing in Figures 4.1-4.3 is most likely due to backscatter interactions, and was reduced when the feature placement (pitch) was increased. While an individual electron may backscatter on the range of microns, a significant density of electrons must backscatter in the same direction for a large enough effective dose of high energy electrons to expose the resist. The observed minimum feature size could thus be a function of this effective dose, suggesting that the distance traveled by backscattered electron with sufficient energy and density to expose the resist is around 100 nm. This relationship is indicated by the graphs in Figure 4.15.

Not explained by proximity dosing is the massive dose required to fully expose the smallest feature widths used, resulting in partially uncleared openings shown in figures 4.6-4.8. This is more likely the result of non-optimized processing parameters such as development time, beam current and shot spacing ($pixels^2$ in equation 7). The parameters used in this project were optimized for Si but not for oxide substrates. Some attempts were made to investigate this but a full study was not undertaken.

Another possible explanation is charging from the electron beam. Like in scanning electron microscopy, insulating samples will build up a negative charge when exposed to the electron beam, causing deflection of the incident electrons and a distortion of the micrograph. In electron beam lithography conducting substrates such as doped Si mediate this problem. Insulating substrates, like un-doped STO, can develop significant surface charge. To mitigate this effect, the conductive polymer ESPACER was used though the relative effectiveness of this treatment compared to other substrates is unknown.

Chapter 5: Conclusions

Electron beam lithography was effectively used to pattern PMMA resists on oxide substrates. While a minimum feature size of 100 nm was observed, smaller features may still be possible. Pulsed Laser Deposition was then used to fill the PMMA templates directly with high yields, removing the need for an etching process when patterning oxide materials. A qualitative estimate of the process yield is greater than 95%, as only edges of the patterned arrays showed any signs of degradation. The large disparity between the EBL software designated dimensions and actual dimensions is likely due to proximity dosing effects, which are increased for insulating substrates with large atomic number.

Future work on this topic should focus on two areas. First, what (if any) improvement of thermoelectric properties is achieved at the current dimensional capability. Films of Nb:STO using PLD have been studied in detail, however these films were grown at conditions optimized for epitaxial growth. As the PMMA templates necessitate the deposition of the oxide material at room temperature, an annealing process is required to crystallize the film. An additional report detailing the work done to characterize room temperature deposited, post annealed films of Nb:STO is presented in Appendix B.

The second approach would be to remove the concerns introduced by using an oxide substrate altogether. The obvious choice for a new substrate would be Si, as it is cheap and already integrated into the semiconductor industry. However, the lattice constant of Si is significant larger than that of STO, making epitaxial growth impossible. Buffer layers have been used for this purpose, and have been grown using PLD. A preliminary study of TiN films and Nb:STO on TiN bilayers is presented in Appendix C.

Bibliography

1. **Rowe, D. M.** *Thermoelectrics Handbook: From Macro to Nano.* Boca Raton : CRC Press, 2006.

2. **H.J. Goldsmid, R.W. Douglas.** The use of Semiconductors in Thermoelectric Refrigeration. *British Journal of Applied Physics.* 1954, Vol. 5, 386.

3. **Rosi, F.D.** Thermoelectricity and Thermoelectric Power Generation. *Solid State Electronics.* 1968, Vol. 11, 833-868.

4. **G.A. Slack, V.G. Tsoukala.** Some Properties of Semiconducting IrSb3. *Journal of Applied Physics.* 1994, Vol. 76, 3.

5. **D.T. Morelli, G.P. Meisner.** Low Temperature Properties of the Filled Skutterudite CoFe4Sb12. *Journal of Applied Physics.* 1994, Vol. 77, 8.

6. **B. C. Sales, D. Mandrus, R. K. Williams.** Filled Skutterudite Antimonides: A New Class of Thermoelectric Materials. *Science.* 1996, Vol. 272, 5266.

7. **G.S. Nolas, G. A. Slack, D. T. Morelli, T. M. Tritt and A. C. Ehrlich.** The effect of rare-earth filling on the lattice thermal conductivity. *Journal of Applied Physics.* 1996, Vol. 79, 8.

8. **T.M. Tritt, G.S. Nolas, G.A. Slack, A.C. Ehrlich, D.J.Gillespie, J.L. Cohn.** Low-temperature transport properties of the filled and unfilled IrSb3. *Journal of Applied Physics.* 1996, Vol. 79, 11.

9. **N. Scoville, C. Bajgar, J. Rolfe, J.P.Fleurial and J. Vandersande.** Thermal Conductivity Reduction in SiGe Alloys By the Addtion of Nanophase Particulates. *Nanostructured Materials.* 1995, Vol. 5, 2.

10. **F. Brochin, B. Lenoir, X. Devaux, R. Martin-Lopez, and H. Scherrer.** Preparation and transport properties of polycrystalline Bi and Bi–SiO2. *Journal of Applied Physics.* 2000, Vol. 88, 6.

11. **R.S. Makala, K. Jagannadham, B.C. Scales.** Pulsed laser deposition of Bi2Te3-based thermoelectric thin films. *Journal of Applied Physics.* 2003, Vol. 94, 6.

12. **J. Tan, K. Kalantar-zadeh, W. Wlodarski, S. Bhargava, D. Akolekar.** Thermoelectric properties of bismuth telluride thin films deposited by radio frequency magnetron sputtering. *Smart Sensors and Actuators.* 2005, Vol. 5836.

13. **F. Zahid, R. Lake.** Thermoelectric properties of Bi2Te3 atomic quintuple thin films. *Applied Physics Letters.* 2010, Vol. 97, 212102.

14. **L.W. Hirano, T. Whitlow.** Superlattice Applications to Thermoelectricity. *Journal of Applied Physics.* 1995, Vol. 78, 9.

15. **A. Shakori, J.E. Bowers.** Heterostructure integrated thermionic coolers. *Applied Physics Letters.* 1234, 1997, Vol. 71, 9.

16. **X. Fang, G. Zheng, C. LaBounty, J.E. Bowers, E. Croke, C.C. Ahn, S. Huxtable, A. Majumdar, A. Shakouri.** SiGeC/Si superlattice microcoolers. *Applied Physics Letters.* 1580, 2001, Vol. 78, 11.

17. **R. Venkatasubramanian, E. Silvola, T. Colpitts, B. O'Quinn.** Thin-Film Thermoelectric Devices with High Room-Temperature Figures of Merit. *Nature.* 597, 2001, Vol. 413, 11.

18. **X. Sun, Z. Zhang, and M. S. Dresselhaus.** Theoretical modeling of thermoelectricity in Bi nanowires. *Applied Physics Letters.* 4005, 1999, Vol. 74, 26.

19. **M.S. Sander.** Fabrication of High-Density, High Aspect Ratio, Large-Area Bismuth Telluride Nanowire Arrays by Electrodeposition into Porous Anodic Alumina Templates. *Advanced Materials.* 665, 2002, Vol. 14, 9.

20. **C. Frantz, N. Stein, L. Gravier, S. Granville, C. Boulanger.** Electrodeposition and Characterization of Bismuth Telluride Nanowires. *Journal of Electronic Materials.* 2043, 2009, Vol. 39, 9.

21. **D. Li, Y. Wu, R. Fan, P. Yang, A. Majumdar.** Thermal conductivity of Si SiGe superlattice nanowires. *Applied Physics Letters.* 3186, 2003, Vol. 83, 15.

22. **A. Boukai, Y. Bunimovich, J. Tamir-Kheli, J.K. Yu, W. A. Goddard, J.R. Heath.** Silicon nanowires as efficient thermoelectric materials. *Nature.* 168, 2007, Vol. 451.

23. **K. Koumoto, Y. Wang, R. Zhang, A. Kosuga, R. Funahashi.** Oxide Thermoelectric Materials: A Nanostructuring Approach. *Annual Review of Materials Research.* 363, 2010, Vol. 40.

24. **K.H. Lee, S.W. Kim, H. Ohta, K. Koumoto.** Ruddlesden-Popper phases as thermoelectric oxides: Nb-doped SrO(SrTiO3)n (n=1,2). *Journal of Applied Physics.* 2006, Vol. 100, 063717.

25. **Y. Wang, K.H. Lee, H. Ohta, K. Koumoto.** Thermoelectric properties of electron doped SrO(SrTiO3)n (n=1,2). *Journal of Applied Physics.* 2009, Vol. 105, 103701.

26. **N. Wang, L. Hana, H. Hea, Y. Ba, K. Koumoto.** Effects of mesoporous silica addition on thermoelectric properties of Nb-doped. *Journal of Alloys and Compounds.* 308, 2010, Vol. 497.

27. **N. Wang, H. Li, Y. Ba, Y. Wang, C. Wan, K. Fujinami, K. Koumoto.** Effects of YSZ Additions on Thermoelectric Properties of Nb-Doped Strontium Titanate. *Journal of Electronic Materials.* 1777, 2010, Vol. 39, 9.

28. **N. Wang, H. He, Y. Ba, C. Wan, K. Koumoto.** Thermoelectric properties of Nb-doped SrTiO3 ceramics enhanced by Potassium Titanate Nanowires Addition. *Journal of the Ceramic Society of Japan.* 1098, 2010, Vol. 118, 11.

29. **Y. Wang, K. Fujinami, R. Zhang, C. Wan, N. Wang, Y. Ba, K. Koumoto.** Interfacial Thermal Resistance and Thermal Conductivity in Nanograined SrTiO3. *Applied Physics Express.* 031101, 2010, Vol. 3.

30. **S. Ohta, T. Nomura, H. Ohta, K. Koumoto.** High-temperature carrier transport and thermoelectric properties of heavily La or Nb doped Single Crystals. *Journal of Applied Physics.* 034106, 2005, Vol. 97.

31. **K. Fukushima, S. Shibagaki.** Nb doped SrTiO thin films deposited by pulsed laser ablation. *Thin Solid Films.* 238, 1998, Vol. 315.

32. **T. Zhao, H. Lu, F. Chen, S. Dai, G. Yang, Z. Chen.** Highly conductive Nb doped SrTiO3 epitaxial thin films grown by laser molecular beam epitaxy. *Journal of Crystal Growth.* 451, 2000, Vol. 212.

33. **K. Fukishima, S. Shibagki.** Niobium Doping Effect on Resistivity of Epitaxially Grown Nb-STO Thin Films by Laser Ablation Method. *Journal of Electroceramics.* 81, 1999, Vol. 4, S1.

34. **W. Ramadan, S. B. Ogale, S. Dhar, S. X. Zhang, D. C. Kundaliya, I. Satoh, T. Venkatesan.** Substrate-induced strain effects on the transport properties of pulsed laser deposited Nb-doped SrTiO3 films. *Applied Physics Letters.* 142903, 2006, Vol. 88.

35. **H. Ohta, S. Kim, Y. Mune, T. Mizoguchi, K. Nomura, S. Ohta, T. Nomura, Y. Nakanishi, Y. Ikuhara, M. Hirano, H. Honso, K. Koumoto.** Giant thermoelectric Seebeck coefficient of a two-dimensional electron gas in SrTiO3. *Nature Materials.* 129, 2007, Vol. 6.

36. **Ohta, H.** Thermoelectrics based on SrTiO3. *Materials Today.* 44, 2007, Vol. 10, 10.

37. **K. Nagashima, T. Yanagida, H. Tanaka, T. Kawai.** Epitaxial growth of MgO nanowires by pulsed laser deposition. *Journal of Applied Physics.* 124304, 2007, Vol. 101.

38. **J. Bae, J. Hong, W.H. Han, Y.J. Choi, R.L. Snyder.** Superior field emission properties of ZnO nanocones synthesized by pulsed laser deposition. *Chemical Physics Letters.* 260, 2009, Vol. 475.

39. **S. Karthauser, E. Vasco, R. Dittmann and R.Waser.** Fabrication of arrays of SrZrO3 by Pulsed Laser Deposition. *Nanotechnology.* S122, 2004, Vol. 15.

40. **Y. Akita, Y. Sugimoto, K. Kobayashi, T. Suzuki, H. Oi, M. Mita, M. Yoshimoto.** Crystal Growth Control of Functional Oxide Thin Films on Nanopatterened Substrate Surface. *Journal of Laser Micro/Nanoengineering.* 202, 2009, Vol. 4, 3.

41. **J.J. Urban, W. S. Yun, Q. Gu, H. Park.** Synthesis of Single-Crystalline Perovskite Nanorods Composed of Barium Titanate and Strontium Titanate. *Journal of the American Chemical Society.* 1186, 2002, Vol. 124, 7.

42. **U.A. Joshi, J. S. Lee.** Template-Free Hydrothermal Synthesis of Single-Crystalline Barium Titanate and Strontium Titanate Nanowires. *Small.* 1172, 2005, Vol. 1, 12.

43. **W. Xu, Y. Shi, H. Hadim.** The Fabrication of Thermoelectric LSCO nanofibers and Seebeck Coefficient Measurment. *Nanotechnology.* 2010, Vol. 21, 395303.

44. **C. H. Bae, S. M. Park, S. C. Park, J. S. Ha.** template, Array of ultraviolet luminescent ZnO nanodots fabricated by pulsed laser deposition using an anodic aluminum oxide. *Nanotechnology.* 381, 2006, Vol. 17.

45. **Broers, A.N.** Resolution Limits of PMMA Resist for Exposure with 50 kV Electrons. *Journal of the Electrochemical Society.* 166, 1981, Vol. 128, 1.

46. **S. Thoms, D.S. Macintyre, M. McCarthy.** Sub 35 nm Metal Gratings Fabricated Using PMMA with High Contrast Developers. *Microelectronic Engineering.* 207, 1998, Vol. 41/42.

47. **F. Yaghmaie, J. Fleck, A. Gusman, R. Prohaska.** Improvement of PMMA electron-beam lithography performance in metal liftoff through a poly-imide bi-layer system. *Microelectronic Engineering.* 2629, 2010, Vol. 87.

48. **S. Xu, Y. Ding, Y. Wei, H. Fang, Y. Shen, A.K. Sood, D. L. Polla, Z.L. Wang.** Patterned Growth of Horizontal ZnO Nanowire Arrays. *Joural of the American Chemical Society.* 6670, 2009, Vol. 131.

49. **H.L. Zhou, A. Chen, L.K. Jian, K.F. Ooi, G.K.L. Goh, K.Y. Zang, S.J. Chua.** Template-directed selective growth of ordered ZnO nanostructures on GaN by the hydrothermal method. *Journal of Crystal Growth.* 3626, 2008, Vol. 310.

50. **T. Sun, Z. Pan, V.P. Dravid, Z. Wang, M. Yu, J. Wang.** Nanopatterning of multiferroic BiFeO3 using “soft” electron beam lithography. *Applied Physics Letters.* 163117, 2006, Vol. 89.

51. **P. Morales, M. DiCiano, and J. Y. T. Wei.** Selective epitaxial growth of submicron complex oxide structures by amorphous SrTiO3. *Applied Physics Letters.* 192509, 2005, Vol. 86.

52. **OverlordQ.** Atomic Force Microscopy Block Diagram. *Wapedia.* [Online] June 10, 2010. [Cited: March 1, 2011.] http://wapedia.mobi/en/File:Atomic_force_microscope_block_diagram.svg.

53. **Keithley Instruments, Inc.** Four-Probe Resistivity and Hall Voltage Measurments with the Model 4200-SCS. *Application Note Series.* Cleveland : Keithley Instruments, Inc. , 2004. 2475.

54. **Owen, G.** Methods for proximity effect correction in electron lithography. *Journal of Vacuum Science and Technology B.* 1889, 1990, Vol. 8, 6.

55. **Acarlso3.** Stranski-Krastanov Growth. *Wikipedia.* [Online] December 4, 2007. [Cited: April 7, 2011.] http://en.wikipedia.org/wiki/File:GrowthModes.png.

56. **Ü. Özgür, Ya. I. Alivov, C. Liu, A. Teke, M. A. Reshchikov, S. Doğan, V. Avrutin,.** A comprehensive review of ZnO materials and devices. *Applied Physics Reviews.* 2005, Vol. 98.

57. **N.C. Shukula, H.H. Liao, J.T. Abiade, M. Murayama, D. Kumar, S.T. Huxtable.** Thermal transport in composites of self-assembled nickel nanoparticles embedded in Yttira Stabilized Zirconia. *Applied Physics Letters.* 2009, Vol. 94, 151913.

58. **R.Q. Guo, J. Nishimura, M. Matsumoto, D. Nakamura, T. Okada.** Catalyst-free synthesis of vertically-aligned ZnO nanowires by nanoparticle-assited pulsed laser deposition. *Applied Physics A.* 843, 2008, Vol. 93.

59. **C. Wang, M.H. Kyder.** Epitaxial Growth of SrTiO3 Thin Films on TiN/Si Substrates using RF Sputtering. *Materials Research Society Symposia Proceedings.* 2007, Vol. 966, 0966-T07-21.

60. **W. Xiang, R. Dong, D. Lee, S. Oh, D. Seong, H. Hwang.** Heteroepitaxial growth of Nb-doped SrTiO3 films on Si substrates by Pulsed Laser Deposition for Resistance Memory Applications. *Applied Physics Letters.* 2007, Vol. 90, 052110.

61. **J.H. Hao, J. Gao, H.K. Wong.** Laser molecular beam epitaxy growth and properties of SrTiO thin films for Microelectronics Applications. *Thin Solid Films.* 559, 2006, Vol. 515.

62. **R. Krishnan, T. Matthews, A.K. Balamurugan, S. Dash, A.K. Tyagi, B. Raj, V. Jayaram.** Reactive Pulsed Laser Deposition of titanium nitride thin film: Optimization of process parameters using Secondary Ion Mass Spectrometry. *Applied Surface Science.* 3077, 2010, Vol. 256.

63. **H.D. Gu, K.M. Leung, C.Y. Chung, X.D. Han.** Room-temperature growth of high-purity titanium nitride by laser ablation of titanium in a nitrogen atmosphere. *Surface Coatings and Technology.* 153, 1998, Vol. 110.

64. **S.H. Kim, H. Park, K.H. Lee, S.H. Jee, D.J. Kim, Y.S. Yoon, H.B. Chae.** Structure and mechanical properties of titanium nitride thin films grown by reactive pulsed laser deposition. *Journal of Ceramic Processing Research.* 49, 2009, Vol. 10, 1.

Appendix A Filled Templates Annealed before Liftoff

Below are images of a filled template identical to template 4 that was annealed and then soaked in acetone for the resist liftoff. A film shell is seen partially obscuring the wires, suggesting that some of the resist baked out preventing a proper liftoff of the film.

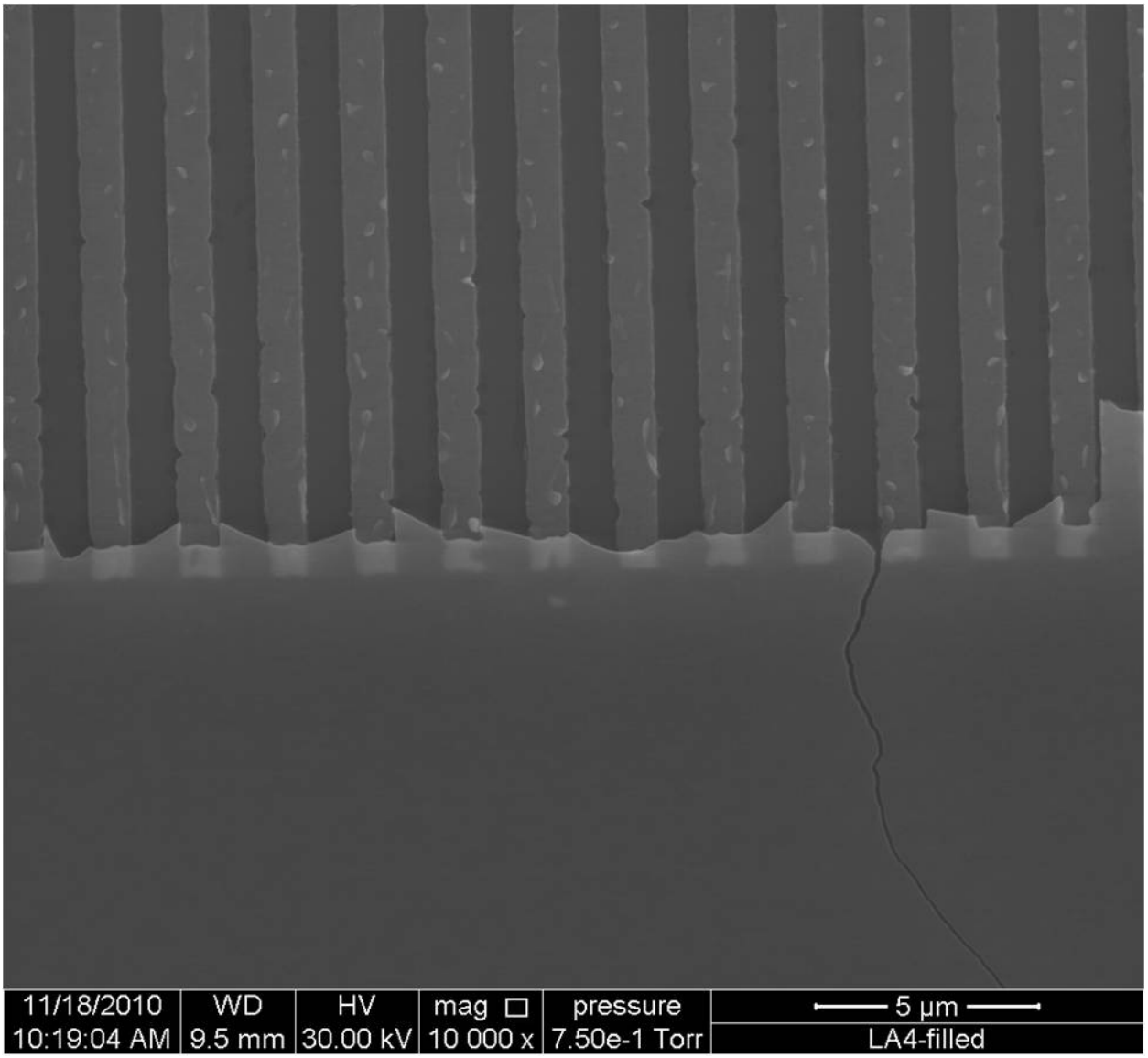

Figure A1 Filled and Annealed Template 4

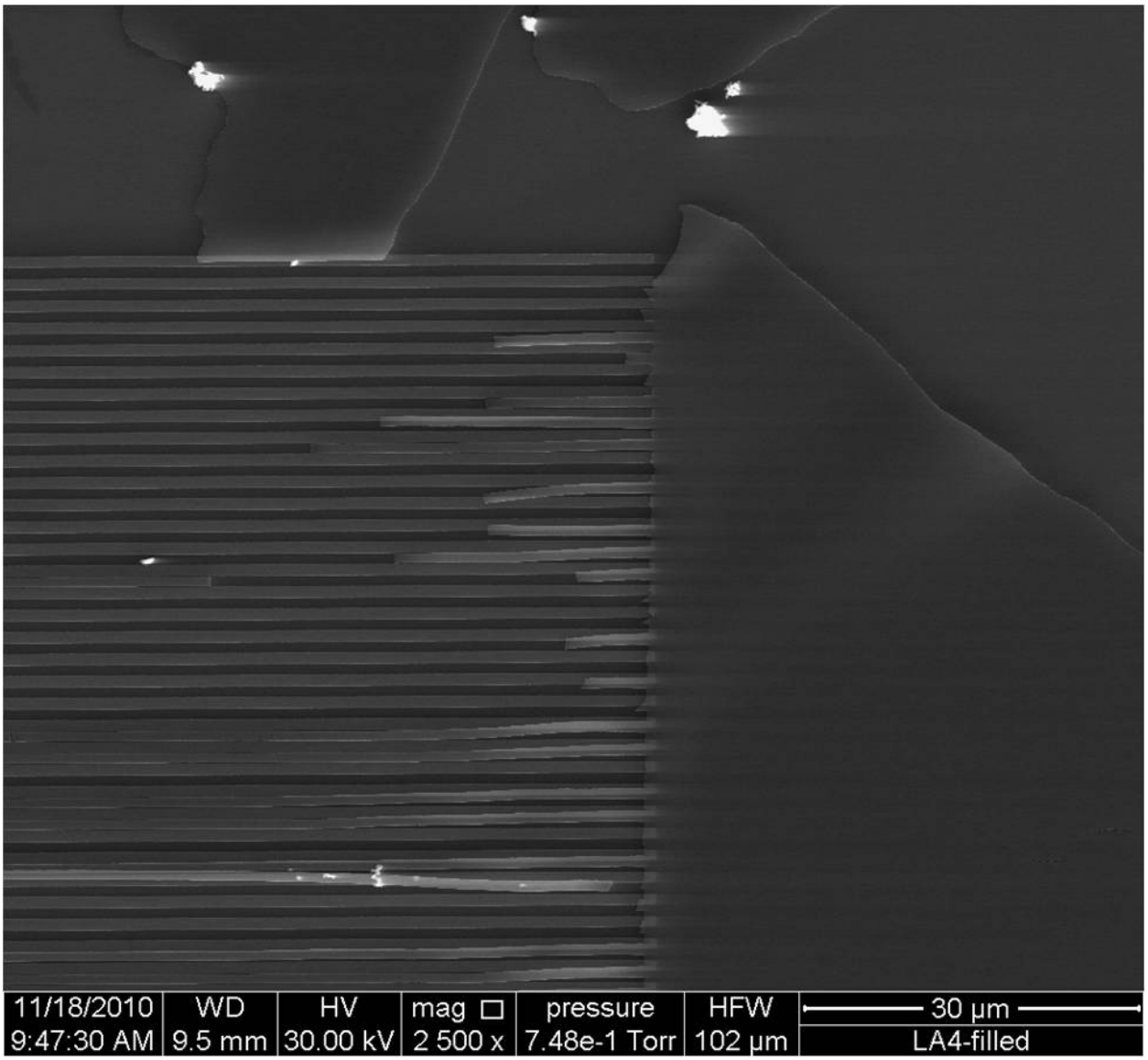

Figure A2 Filled and Annealed Template 4

Appendix B NbSTO Film Study

$SrTi_{.8}Nb_{.2}O_3$ films were deposited onto single crystalline STO and LAO substrates to serve as benchmarkss for the oxide nanostructures. Crystallinity, composition, surface roughness and electrical conductivity were used to quantify the film quality. The film analogues were necessary as the PMMA templates are unable to withstand the temperatures normally used for the growth of epitaxial oxide films using PLD. Films were deposited at 650 °C in high vacuum to serve as benchmarks for films that were deposited at room temperature and subsequently annealed. The annealing profile used for the films was identical to that used during the deposition of films at high temperature, and is displayed in Figure B1. During a high temperature deposition, ablation occurs during the 20 minutes at 650 °C period.

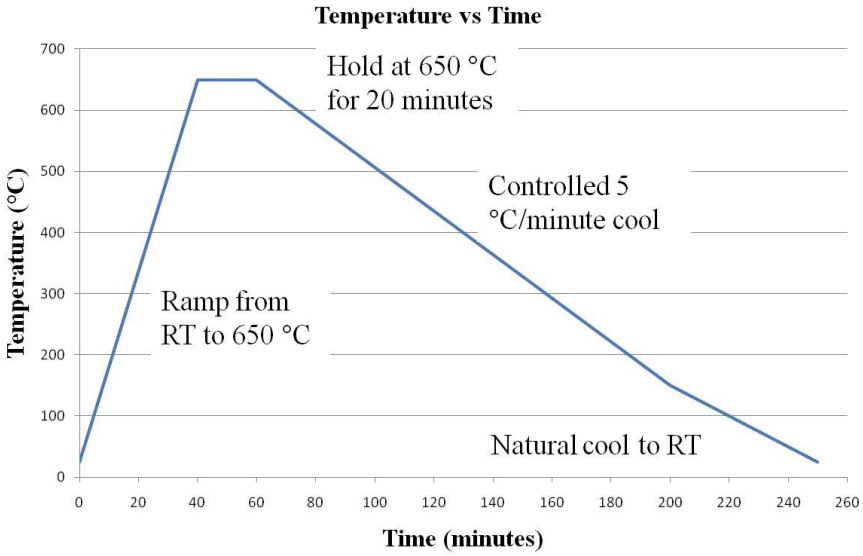

Figure B1 Nb:STO Heat Schedule

B-1 Film Crystallinity

X-ray Diffraction studies reveal that as expected, crystalline films of $SrTi_{.8}Nb_{.2}O_3$ were formed during high temperature deposition onto LAO.While STO substrates were used for the templates, LAO substrates were used when depositing films for XRD, as the peaks of the STO and $SrTi_{.8}Nb_{.2}O_3$ films are nearly coinciding. Room temperature deposited films showed no crystalline peaks in addition to those of the substrate. After annealing, additional peaks were observed but at shifted values and lower intensity compared high temperature deposition, indicating a change in lattice constant, shown in Figure B2.

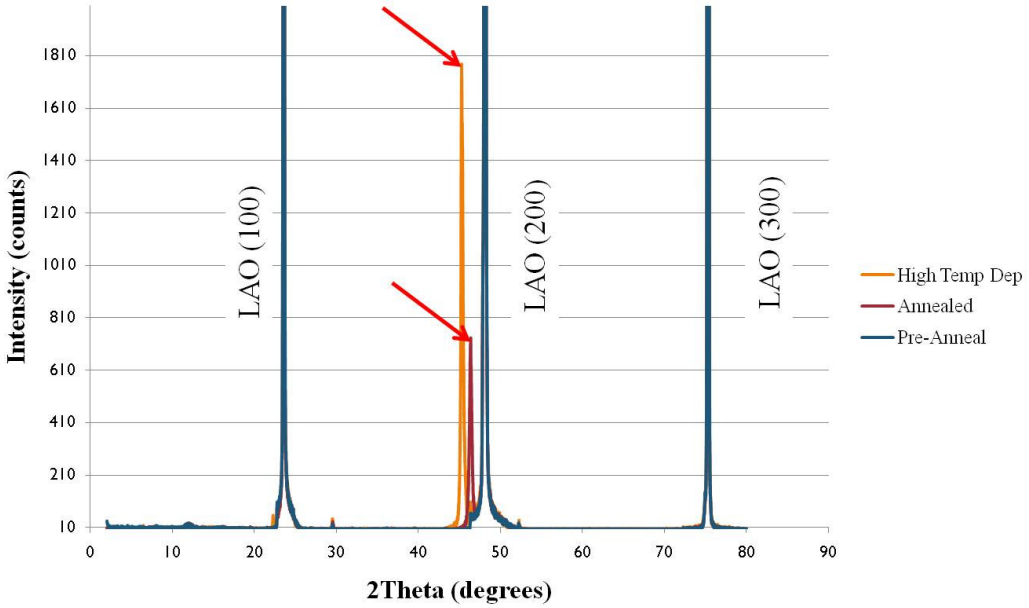

Figure B2 XRD of $SrTi_{.8}Nb_{.2}O_3$ Films

Using the Bragg Equation (Eq. 8), the lattice constants for the two films and the substrate were calculated, shown in Table B1

Table B1: Lattice Constants of $SrTi_{.8}Nb_{.2}O_3$ Films

Sample	2Theta (degrees)	D (Å)
HT deposition	**45.25**	**4.01**
RT then annealed	**46.35**	**3.92**
LAO substrate	**48**	**3.79**

Average grain size can be calculated for the same XRD data using the Scherrer Equation (Eq. 9), shown in Table B2, where FWHM is the full width at half maximum (β) value. Grain size values are close, suggesting the extent of crystallization achieved during annealing is comparable to that of the high temperature deposited film.

Table B2 Average Grain Size using Scherrer Equation

Sample	2Theta(Degrees)	FWHM (radians)	Avg. Grain Size (nm)
RT Then Annealed	46.35	0.32873	26.3
HT deposition	45.25	0.26637	32.3

B-2 Surface Roughness

Contact mode AFM was used to measure surface roughness of the deposited films. An epitaxial film should have a very low surface roughness and be generally featureless. For each sample, three 5 x 5 μm areas were scanned. For very smooth samples, a bowing effect is observed which causes a miscalculation of the average roughness, R_a, which is simply the average of the absolute values for all measured displacements. Bowing can be seen as a white edge on the right hand side of the bare substrate and high temperature deposited film AFM images. To avoid this, a smaller 2 x 2 μm sample box is selected within the 5 x 5 μm scan area and used to calculated average roughness. Table B3 displays the average roughness and standard deviation for the high temperature deposited, room temperature deposited and then annealed, and a bare LAO substrate. Bowing was not observed for the annealed film and thus the R_a value displayed is calculated for the full 5 x 5 μm area. AFM images of these three films are shown in Figure B3.

Table B3 Surface Roughness of Nb:STO Films

Sample	Average Roughness, Ra (nm)	Standard Deviation (nm)
LAO substrate	0.065	-
HT deposition	0.231	0.481
RT Then Annealed	2.600	1.612

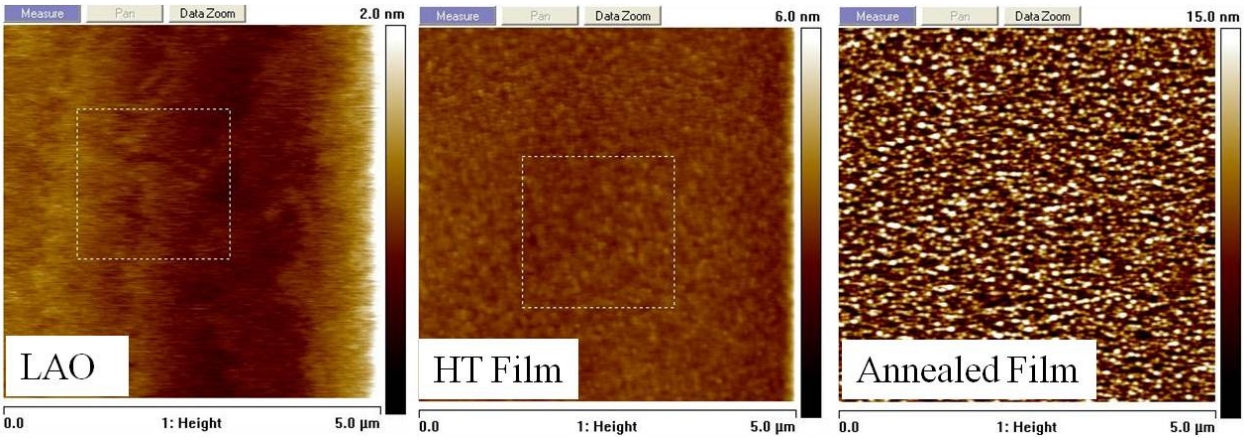

Figure B3 AFM images of Films

The difference between the annealed and high temperature deposited film is fairly dramatic. The relative smoothness of the high temperature film and the featureless surface, combined with the XRD data suggest that it is an epitaxial film. For the annealed film, uniform but discrete islands are observed. Most likely the deposited material becomes frozen to the substrate as amorphous particles, and then crystallizes during annealing but lacks the kinetic energy to form into a film. Furthermore, the approximate size of the largest particles shown in the AFM image is about 50 nm, which is on the same order of magnitude of the crystallite size calculated in section B1.

B-3 Film Composition

XPS sputter depth profiles provided composition analysis for a high temperature deposited film and an annealed room temperature deposited film. Sputter rates were calculated using a known sputtering time and depth measurements of the sputter crater using a profilometer. This was then used to plot composition vs depth into the film. For films deposited at high temperature in vacuum, no diffusion of Nb is evident, and the films are stoichiometric to the ablation targets nominal composition of 5 atm% Nb, shown in Figure B4. Carbon can be seen as a contaminant in the first several nm, which is considered surface contamination and not part of the film structure. In the film the concentration of Nb is constant, and then drops to 0 atm% at once the substrate is reached. Also apparent is the increase in oxygen concentration at the interface between the film and the substrate, which occurs at around 100 nm. This is likely due to the presence of oxygen vacancies which form during PLD deposition of oxide films in vacuum.

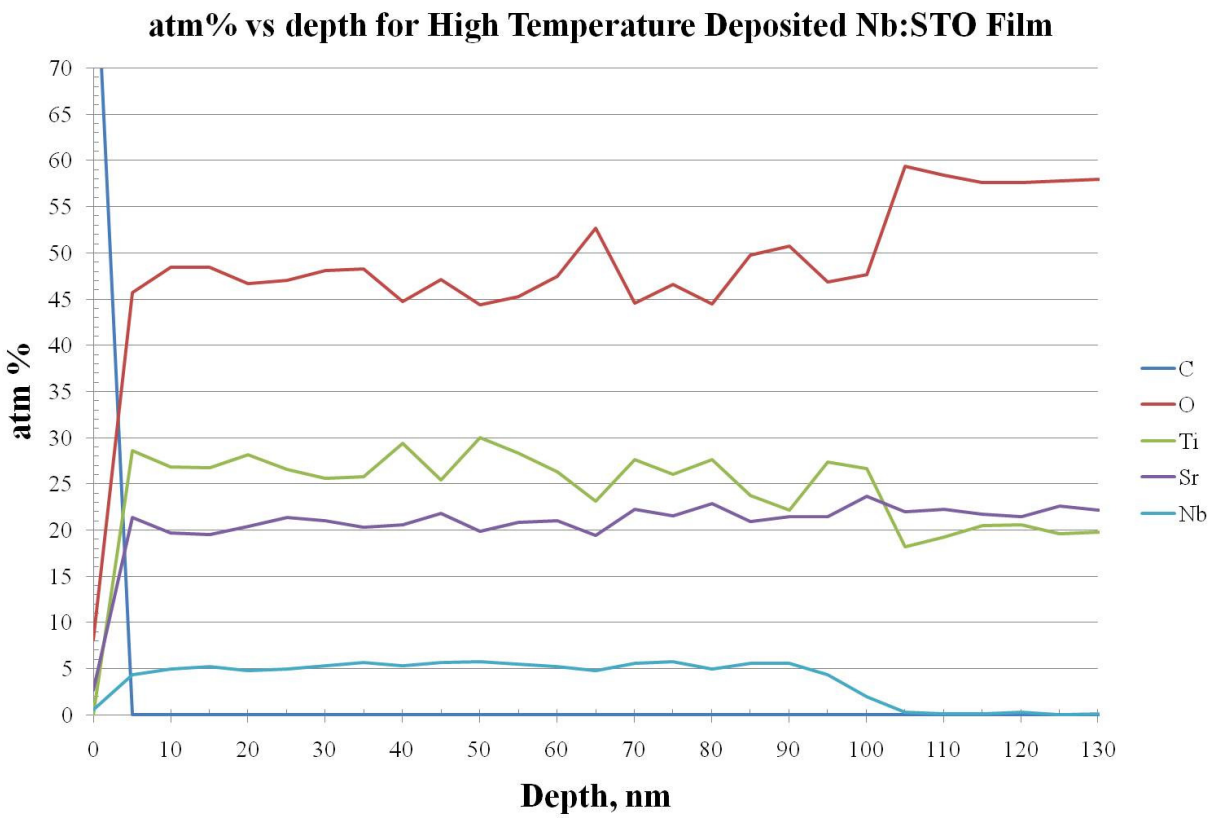

Figure B4 XPS Sputter Depth Profile for High Temperature deposited NbSTO Film

While the XRD and AFM results suggest there is a structural difference between annealed and high temperature deposited samples, a compositional change is not observed in XPS analysis of the annealed samples shown in Figure B5. In fact, the compositions of Ti, Sr and O are much more consistent, suggesting the deposited film is more stable with a room temperature substrate. No diffusion of the Nb dopant atom into the STO substrate is observed, reinforcing the evidence that the change in lattice constant is due to a crystallite shape change and not a change in composition.

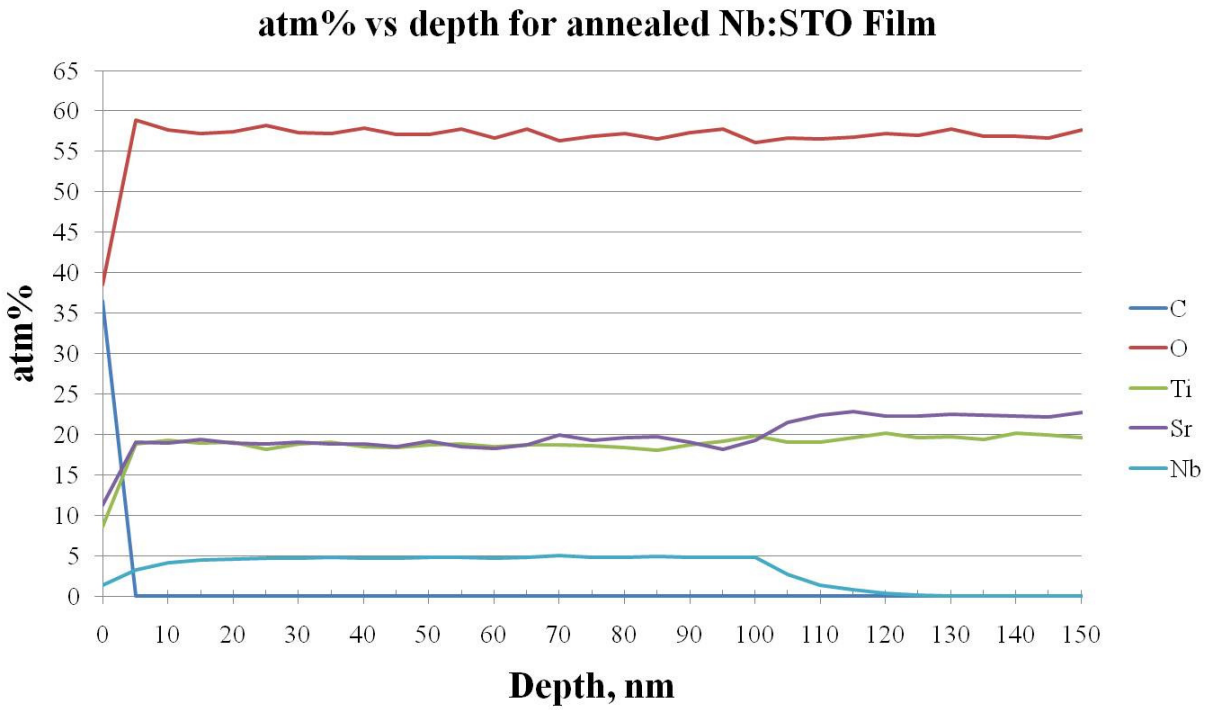

Figure B5 XPS Sputter Depth Profile for annealed NbSTO Film

B-4 Electrical Conductivity

Electrical conductivity of films and substrates was conducted using the van der Pauw 4 point probe method. The results from these tests are summarized in Table B4.

Table B4 Electrical Conductivity of NbSTO Films

Sample	Electrical Conductivity (Ω cm)	Standard Deviation
HT NbSTO	1.81E-04	2.65E-05
Annealed NbSTO	1.43E+00	6.08E-2
RT NbSTO	3.74E+02	9.67E+01
STO Substrate	1.00E+08	-

While all of the deposited films are several orders of magnitude more conductive than the bare STO single crystalline substrate, growth temperature has an obvious impact. Standard deviation is not available for the bare STO as in all measured areas conductivity exceeded the capable range of the

measurement apparatus, reporting the maximum value. The film deposited at 650 °C (HT NbSTO) is the most conductive with conductivity on the order of 10^{-4} Ω cm, which is consistent with the results reported by Zhao et. Al (32). While the annealed film shows some improvement in electrical conductivity over the un-annealed room temperature deposited film it is still much more insulating than the high temperature case, suggesting the annealing treatment is not entirely effective at restoring the properties observed for the high temperature deposited films.

B-5 Conclusions

The heat treatments used to simulate the post processing for the patterned oxides were successful on all accounts. Annealed samples became crystalline, electrical conductivity improved by two orders of magnitude, and no diffusion of the Nb dopant was evident from XPS sputter depth profiles. However, the annealing of room temperature deposited films proved insufficient to produce films of epitaxial quality. From the analysis of the XRD spectrum using the Bragg equation, a slight shift in lattice constant is observed. Furthermore, the surface roughness from AFM measurements show that while the high temperature deposited film is smooth to the sub nanometer level, the annealed film is covered in spherical nanograins on the same scale calculated from the XRD results using the Scherrer equation.

Thin film growth can be categorized into three growth modes, namely Volmer-Weber or island growth, Frank van-der-Merwe or layer by layer growth and Stanski-Krastanov or layer plus island growth. The three growth modes are depicted in Figure 5.2 in which Volmer-Weber is (a), Fank van-der-Merwe is (b) and Stanski-Krastanov is (c) (55). For epitaxial growth, the Frank van-der-Merwe growth mode is preferred. Films grown layer by layer are characterized by their low surface roughness and single phase diffraction patterns. Critically important to the occurrence of layer by layer growth (and thus the formation of an epitaxial film) is the interfacial tensions between the nucleating film (a liquid) and the substrate, the ambient vapor from which the film condenses and the substrate, and between the nucleating film and the ambient vapor. These surface tensions are described by Young's Equation (Equation 18) in which γ_{SL} is the surface energy between the substrate and film, γ_{LV} is the surface energy between the film and the vapor species and γ_{SV} is the surface energy between the substrate and the ambient vapor. The angle formed between the film nuclei and the substrate, θ, is known as the contact or wetting angle.

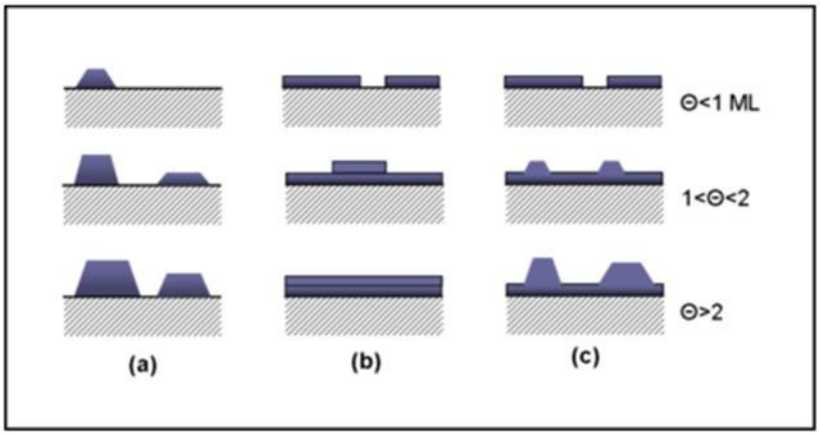

Figure B6 Thin Film Growth Modes

$$\gamma_{SL} + \gamma_{LV} cos\theta = \gamma_{SV} \qquad (Eq. 19)$$

Equation 18 represents an equilibrium condition in which the chemical potential of the three phases are equal, and the resulting contact angle dictates the prevailing growth mode. A large contact angle yields island growth whereas a contact angle of zero leads to layer by layer growth. During Stranski-Krastanov growth the contact angle increases during growth due to changes in lattice constant, eventually reaching a critical point when islands form on top of previously deposited layers.

As a persistent vapor species is not formed during PLD, the traditional growth modes are somewhat inaccurate. Instead what is typically observed during PLD growth of films is a growth mode analogous to the island mode. In the island growth mode, discrete islands nucleate and eventually converge, forming films. Instead of the islands nucleating form a vapor species, they arrive at the substrate as particulates during PLD (56). For this reason PLD has been capitalized upon to form freestanding nanoparticles or for application as precursors for vapor-liquid-solid growth of nanowires (57) (58). When the lattice strain is low and the substrate temperature is high, epitaxial films will form by migration of these particulates. In the case of the room temperature deposition the particulates are frozen in place, and while annealing causes them to crystallize they do not form into smooth films. Hence, the continuity of the conducting layer is reduced, negatively effecting electrical conductivity and the crystallites form under differing strain conditions from the high temperature film resulting in a modified lattice constant. This particle aggregation may also be the cause of the surface roughness of the nanowires when observed using AFM. Another possible explanation for the large conductivity of the high temperature deposited film is indicated by the low oxygen concentration observed in XPS. Oxygen vacancies serve as n-type dopants, as the absence of a single oxygen ion leaves several unbound (free) electrons which contribute to electrical conductivity.

Appendix C TiN Films on Si

Due to the larger than expected feature width during EBL patterning of the STO substrates, as well as the possibility of diffusion of the Nb dopant atoms into the STO substrate merit investigation into alterative substrate choices for NbSTO films. Titanium Nitride (TiN) has been demonstrated as an effective intermediate layer for depositing STO and NbSTO on Si (100) substrates (59) (60). With a nominal lattice spacing for (100) oriented TiN of 4.24 Å, TiN can effectively mitigate epixatial strain induced by a Si (100) substrate with a lattice constant of 5.43 Å. While NbSTO can be grown epitaxially on Si (100), a crystallographic rotation in reference to the substrate observed only at high temperature is necessary to avoid the formation of a polycrystalline film (61). Furthermore, TiN has been grown using PLD and a pure Ti target in method known as "reactive pulsed laser deposition" in which the ablated species combines with a reactant gas to form a new species in situ. Several experimental parameters are optimized for this approach, though a number of successful attempts have been demonstrated (62) (63) (64). Films of TiN were deposited on Si(100) substrates at 300 °C in a partial pressure of $2x10^{-3}$ Torr of nitrogen. Repetition rate and laser energy were increased per the literature sources results to 10 Hz and 5 J/cm^2 respectively. For films of pure TiN 20000 laser pulses were used. NbSTO films were also deposited on top of TiN films deposited at the aforementioned parameters. These films were deposited at room temperature in high vacuum (10^{-6} Torr) and then annealed using the heat treatment described in section 4.2. The bilayer films were depisted with 10000 pulses of TiN and nominally 100 nm of NbSTO. Both monolayer and bilayer films were characterized using AFM, XRD, and van der Pauw method. A bilayer film was also subjected to an XPS sputter depth profile.

C-1 Film Crystalinity

XRD analysis of the NbSTO on TiN bilayer revealed no crystalline peaks indexed to any phase of TiN or NbSTO, suggesting that the PLD parameters used for growth of the TiN layer were incorrect. Literature sources cite using a 10 J/cm^2 energy density or higher however the maximum energy density cable of the PLD system used was 5 J/cm^2.

C-2 Surface Roughness

TiN films showed similar roughness levels as the oxide films discussed in section 4.2. Interestingly, when an Nb:STO film was deposited at room temperature and annealed the particulate morphology seen when using the oxide substrate was not observed. Instead, a slightly larger average roughness but generally featureless surface is observed. The roughness values are found in Table 4.7, and the AFM micrographs in figure 4.22. As with the Nb:STO films in section 4.2, subselections of the AFM

micrograph were used when measuring surface roughness to avoid the contribution of bowing in the piezoelectric sample mount.

Table C1 Surface Roughness of TiN Films

Sample	Average Roughness, Ra (nm)	Standard Deviation (nm)
Si Substrate	0.377	-
TiN on Si	0.505	0.018
Nb:STO on TiN on Si	0.575	0.071

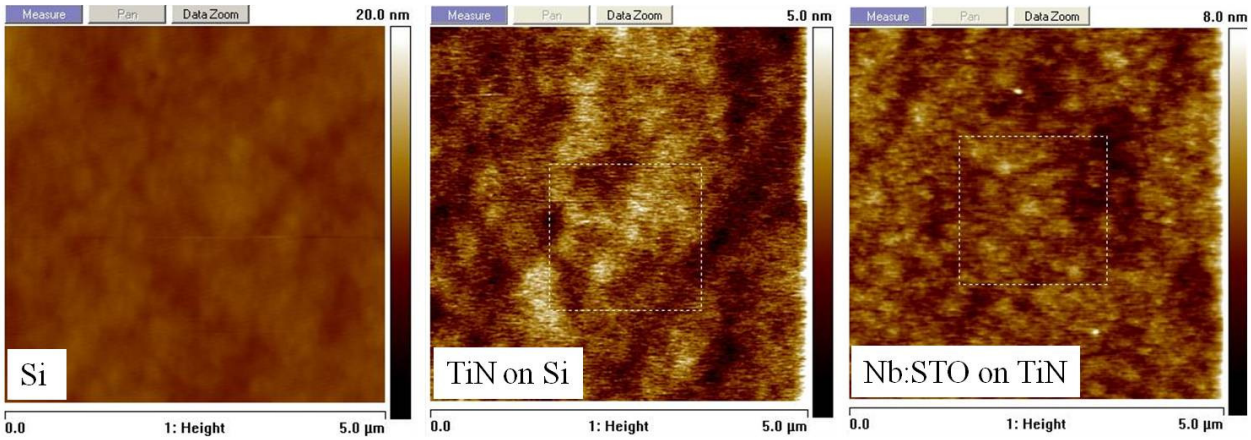

Figure C1 AFM on TiN Films

C-3 Composition

XPS results of the TiN and Nb:STO bilayers do show a clear transition between the doped oxide top film and the TiN buffer layer. However, while the Ti and N concentration increase at the same depth as when the Nb and Sr drop, O concentrations remain relatively constant. This suggests that while deposited in a pure nitrogen atmosphere into a vacuum chamber with a 10^6 Torr base pressure, significant oxidation of the Ti atoms has occurred. Whether this oxidation is due to contribution from the oxide film, the surface of the Si substrate or residual oxygen in the reaction chamber is unknown. The low concentration of N also suggests that the deposited film is a combination of TiN, TiO_x and perhaps pure Ti. The XPS sputter depth profile is shown in figure 4.23. The sputter rate for TiN is assumed equal to the calculated sputter rate of the oxide film.

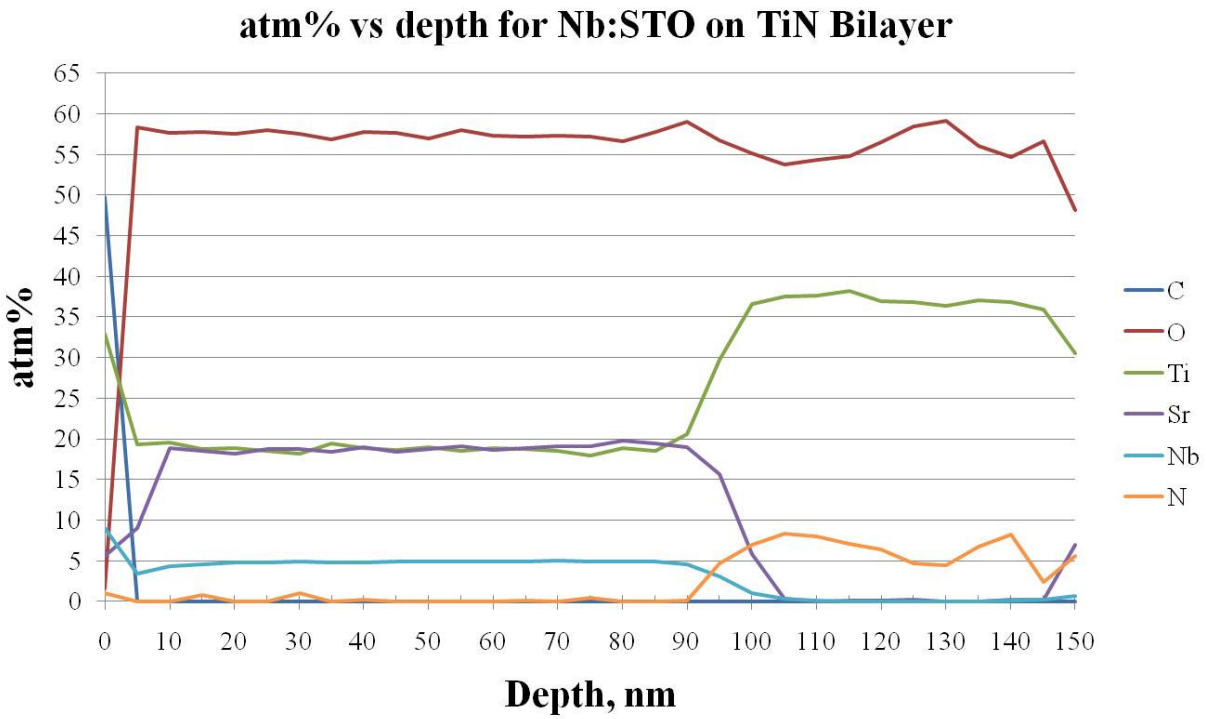

Figure C2 XPS Sputter Depth Profile on Nb:STO on TiN Bilayer film

C-4 Electrical Conductivity

The boron doped Si substrates, 300 °C deposited TiN films and annealed Nb:STO films on TiN films were tested for electrical conductivity with results displayed in Table 4.8. These films show significantly increased conductivity compared to the annealed films on oxide substrates. For the Si substrates, the vendor reported conductivity was 20 Ω-cm.

Table C2 Electrical Conductivity of TiN Films

Sample	Electrical Conductivity (Ω cm)	Standard Deviation
Si Substrate	7.55E+00	3.60E+00
TiN on Si	2.41E-05	1.77E-06
NbSTO on TiN on Si	4.82E-03	7.16E-04

C-5 Conclusions

While the electrical conductivity and AFM results suggest the formation of high quality thin films, improper stoichiometricry observed in XPS and a lack of TiN crystalline peaks fail to provide a complete picture. A possible explanation is that pure, polycrystalline Ti was grown on the surface of the Si substrate with minority TiN and TiO_x phases. The relative smoothness of the films may also be a function of an extremely thin film rather than an epitaxial one. This is especially possible as the work presented in references 62-64 used much larger energy densities and repetition rates were required to grow films of only a few hundred nanometers as Ti is not easily ablated. However, the parameters reported are all beyond the capability of the system used for these experiments.